IMAGE DECONVOLUTION METHODS BASED ON FOURIER TRANSFORM PHASE AND BOUNDED ENERGY

A DISSERTATION SUBMITTED TO
THE GRADUATE SCHOOL OF ENGINEERING AND SCIENCE
OF BILKENT UNIVERSITY
IN PARTIAL FULFILLMENT OF THE REQUIREMENTS FOR
THE DEGREE OF
DOCTOR OF PHILOSOPHY
IN
ELECTRICAL AND ELECTRONICS ENGINEERING

By
Onur Yorulmaz
August 2018

IMAGE DECONVOLUTION METHODS BASED ON FOURIER TRANSFORM PHASE AND BOUNDED ENERGY

By Onur Yorulmaz

August 2018

We certify that we have read this dissertation and that in our opinion it is fully adequate, in scope and in quality, as a dissertation for the degree of Doctor of Philosophy.

A. Enis Çetin(Advisor)

Ömer Morgül

Uğur Güdükbay

Ali Ziya Alkar

Cenk Toker

Approved for the Graduate School of Engineering and Science:

Ezhan Karaşan
Director of the Graduate School

ABSTRACT

IMAGE DECONVOLUTION METHODS BASED ON FOURIER TRANSFORM PHASE AND BOUNDED ENERGY

Onur Yorulmaz
Ph.D. in Electrical and Electronics Engineering
Advisor: A. Enis Çetin
August 2018

We developed deconvolution algorithms based on Fourier transform phase and bounded energy. Deconvolution is a major area of study in image processing applications. In general, restoration of original images from noisy filtered observation images is an ill-posed problem. We use Fourier transform phase as a constraint in developed image recovery methods. The Fourier phase information is robust to noise, which makes it suitable as a frequency domain constraint. One of our focus is microscopy images where the blur is caused by slight disturbances of the focus. Because of the symmetrical optical parameters, it may be assumed that the Point Spread Function (PSF) is symmetrical. This symmetry of PSF results in zero phase distortion in the Fourier transform coefficients of the original image. Since the convolution leads to multiplication in Fourier domain, we assume that the Fourier phase of some of the frequencies of observed image around the origin represents the Fourier phase of the original image in the same set of frequencies. Therefore the Fourier transform phases of the original image can be estimated from the phase of the observed image and this information can be used as a Fourier domain constraint. In order to complete the algorithm, we also use a Total Variation (TV) reduction based regularization in spatial domain. We embed the proposed Fourier phase relation and spatial domain regularization as additional constraints in well-known blind Ayers-Dainty deconvolution method. Another problem we focused on is the restoration of highly blurry Magnetic Particle Imaging (MPI) applications. In this study we developed a standalone iterative algorithm. The algorithm again relies on the symmetry property of the MPI PSF. The phase estimates of the true image are obtained from the observed image. In this case we employ an ℓ_1 projection based regularization algorithm. The ℓ_1 projection reduces the small coefficients to zero which is suitable for MPI application because the contrast between foreground and background is sufficiently large by

nature. Finally, a more general restoration algorithm is developed for deconvolution of non-symmetrical filters. The algorithm uses the known Fourier phase properties of the PSF in order to estimate the Fourier transform phase of the original image. We also update the estimated Fourier transform magnitudes iteratively using the knowledge of observed image and the PSF. A TV reduction based regularization method completes the algorithm in spatial domain. Simulations and experimental results show that the proposed algorithm outperforms the Wiener filter. We also conclude that the addition of estimate of Fourier transform phase is useful in any deconvolution method.

Keywords: Microscopy imaging, Magnetic particle imaging, Blind deconvolution, Deblurring, Projection onto Convex Sets, Total Variation reduction.

ÖZET

FOURIER DÖNÜŞÜMÜNÜN FAZI VE SINIRLANDIRILMIŞ ENERJİ TEMELLİ İMGE TERS EVRİŞİM YÖNTEMLERİ

Onur Yorulmaz
Elektrik ve Elektronik Mühendisliği, Doktora
Tez Danışmanı: A. Enis Çetin
Ağustos 2018

Fourier dönüşümün fazı ve sınırlandırılmış enerji tabanlı ters evrişim algoritmaları geliştirilmiştir. Ters evrişim, imge işleme uygulamalarında önemli bir araştırma alanıdır. Genel olarak, gürültülü filtrelenmiş gözlem imgelerinden özgün imgelerin kurtarılması kötü konumlanmış bir problemdir. Geliştirdiğimiz imge kurtarma algoritmalarında Fourier dönüşüm fazını bir kısıtlayıcı olarak kullandık. Fourier faz frekans tanım kümesinde kısıtlayıcı olarak kullanılabilecek kadar gürültüye gürbüzdür. Odaklandığımız konulardan bir tanesi bulanıklık kaynağı odaklamadaki küçük hatalar olan mikroskop imgeleri idi. Optik parametrelerin simetrik olmasından ötürü, Nokta Dağılımı Fonksiyonunun (NDF) simetrik olacağı varsayılabilir. NDF'de gözlemlenen bu simetri, orjinal imgenin Fourier dönüşüm katsayılarında sıfır faz kadar bozulma sonucunu doğurur. Evrişim Fourier tanım kümesinde çarpma işlemine denk geldiği için, gözlemlenen imgenin başlangıç noktası etrafındaki bazı frekanslardaki Fourier fazlarının aynı frekanslardaki orjinal imge Fourier fazlarını temsil edeceğini varsayabiliriz. Sonuç olarak, orjinal imgenin Fourier transform fazları gözlemlenen imgeden tahmin edilebilir ve bu bilgi Fourier tanım kümesinde kısıtlayıcı olarak kullanılabilir. Algoritmayı tamamlamak üzere, buna ek olarak uzaysal tanım kümesinde Toplam Değişme (TD) azaltma tabanlı bir düzenleme algoritması kullanılmıştır. Sunulan bu Fourier faz ilişkisini ve uzaysal tanım kümesinde düzenleme algoritmasını herkesçe bilinen kör Ayers-Dainty ters evrişim yöntemine bir sınırlayıcı olarak ekledik. Odaklandığımız bir başka problem ise oldukça bulanık Manyetik Parçacık İmgeleme (MPİ) uygulamalarında imgelerin kurtarılmasıydı. Bu çalışmamızda tek başına çalışabilen yinelemeli bir algoritma geliştirdik. Algoritma da yine MPİ NDF'nin simetri özelliğini temel almaktadır. Gerçek imgenin tahmini fazı gözlemlenen imgeden elde edilmektedir. Bu çalışmada ℓ_1 izdüşümü tabanlı düzenleme algoritmasından faydalandık. MPİ imgelerinde ön plan ve arka plan

arasında doğal olarak bulunan yeterli yükseklikteki kontrast nedeniyle, küçük katsayıları sıfıra götüren ℓ_1 izdüşümü uygun bir yöntem olarak belirlenmiştir. Son olarak, simetrik olmayan filtreleri ters izdüşümlemek için daha genel bir kurtarma algoritması geliştirilmiştir. Algoritma, orjinal imge Fourier dönüşüm fazlarını tahmin etmek için NDF'nin bilinen Fourier fazı özelliklerinden faydalanmaktadır. Bunun yanısıra gözlemlenen imgenin ve NDF'nin bilgisi kullanılarak Fourier transform büyüklük tahminleri de güncellenmektedir. TD azaltma temelli bir düzenleme yöntemi algoritmayı uzaysal tanım kümesinde tamamlar. Sunulan algoritmanın Wiener filtrelerini başarım açısından geride bıraktığı simülasyon ve deneysel sonuçlarla gösterilmiştir. Ayrıca, Fourier dönüşüm fazının tahmini değerinin ek olarak kullanılmasının, ters evrişim yönteminlerinde faydalı olduğu sonucuna ulaşılmıştır.

Anahtar sözcükler: Mikroskopi imgeleme, Manyetik Parçacık imgeleme, Kör Ters Evrişim, Netleştirme, Konveks Kümelere izdüşümleme.

Acknowledgement

I would like to express my gratitude to Prof. Dr. A. Enis Çetin for his supervision, guidance and suggestions throughout the development of this thesis.

I would also like to thank Prof. Dr. Ömer Morgül, Prof. Dr. Uğur Güdükbay, Prof. Dr. Ali Ziya Alkar, and Assoc. Prof. Dr. Cenk Toker for reading, commenting and making suggestions on this thesis.

I am grateful to Asst. Professors, Dr. Emine Ülkü Sarıtaş and Dr. Tolga Çukur for their contribution to my studies that are included in this thesis.

I would also like to thank to my friends and colleagues Dr. Kıvanç Köse and Mohammad Tofighi for their help and support throughout the development of this thesis. I would especially like to thank my friend Dr. Talya Şans Uçaryılmaz for her support and relentless encouragement.

It is a pleasure to express greatest gratitude to my mother, father, sister and brother-in-law for their sincere love, unparalleled support and encouragement.

Contents

1 Introduction **1**

2 Theory and Methods of the Phase-based Image Restoration **4**

2.1 Fourier Transform Phase 4

2.2 Energy Based Regularization Methods 9

2.2.1 Total Variation Reduction 10

2.2.2 Projections onto ℓ_1 Ball 11

2.3 Projection onto Convex Sets (POCS) 14

2.3.1 Projection onto the Phase Set 14

2.3.2 Approximate Projection onto TV Set 15

2.3.3 Comparison Measure 17

2.4 Summary 17

3 Fourier Transform Phase and Total Variation Based Improvement of Blind Deconvolution Methods **18**

3.1 Previous Studies in Image Quality Enhancement of Microbiology Images 19

3.2 Convex Sets Used in Blind Deconvolution 20

3.2.1 Extraction of Fourier Transform Phase 20

3.2.2 Spatial Domain Sets 22

3.3 Improved Ayers-Dainty Blind Deconvolution Techniques using POCS Method 23

3.4 Experimental Results 26

3.4.1 Blind Deconvolution of 3D images 26

3.4.2 2D Blind Deconvolution with Ayers-Dainty Method 30

3.5 Summary 32

4 Fourier Transform Phase and Bounded Energy-based Deconvolution for Magnetic Particle Imaging 36

4.1 Previous Studies on Magnetic Particle Imaging 37
4.2 Methods 38
4.2.1 Fourier-Domain Phase Constraint 39
4.2.2 Spatial-Domain Support Constraint 42
4.2.3 Spatial-Domain Regularization Constraint 43
4.2.4 The MPI Deconvolution Algorithm 43
4.2.5 Simulated MPI Acquisitions 45
4.3 Simulation and Results 47
4.4 Summary 50

5 Phase-based Iterative Deconvolution 55

5.1 Review of Wiener Deconvolution 55
5.2 TV and Fourier phase based deconvolution method for general filter types 57
5.2.1 Fourier phase constraint 57
5.2.2 TV-based Regularization 59
5.3 Experimental Results 61
5.4 Summary 66

6 Conclusions 72

Bibliography 75

List of Figures

2.1 (a) A noisy version of "Lena" image, (b) reconstruction of "Lena" from FT phase with unit magnitude only and (c) reconstruction of noisy "Lena" from FT phase with unit magnitude only. 5

2.2 Upper half plane (UHP) indices are shown as dark points in (n_1, n_2) plane. The LHP is the bottom part. 7

2.3 (a) The signal x is a 1D signal, (b) y is the filtered version of x with a Gaussian PSF with $\sigma = 1.2$ and, (c) Discrete Fourier Transform (DFT) phase of x and y for a DFT size of 130. 9

2.4 Shaded area represents the first quadrant of the 2D version of ℓ_1 ball. The vector $\mathbf{w}_\mathbf{a}^*$ is the projection of $\mathbf{v}_\mathbf{a}$ onto the ℓ_1 ball. The projection of $\mathbf{v}_\mathbf{b}$ is difficult to compute in high dimensions, but $\mathbf{w}_\mathbf{p}^*$ can be used instead of the projection. 12

3.1 Examples of microscopy imaging PSFs (a) in multiple focus levels and (b) in a single out-of-focus distance ($2\mu m$). In (b) an interference related symmetrical pattern is visible which yields real Fourier domain components. [Image courtesy of Pascal Chartrand, University of Montreal.] 23

3.2 The flowchart of the improved Ayers-Dainty method. 25

3.3 Comparison of deconvolution algorithms: (a) The test image from [1], (b) Observed image blurred by Gaussian filter with $\sigma = 6$. (c) Image deblurred by the non-blind deconvolution method in [1], PSNR = 22.43dB, (d) Image deconvolved by pure Ayers-Dainty method, PSNR = 24.86 dB. (e) Result of the presented phase projection based Ayers-Dainty extension, PSNR = 24.91 dB. (f) Results of Ayers-Dainty method with FT phase and spatial domain projections, PSNR = 25.18 dB. 27

3.4 (a) DAPI stained cell nuclei image (100X) from Huh7 cells with best possible focus: x_f and (b) another image with slight out of focus x_g. The images x_f and x_g are combined to obtain (c) the deblurred image using Gaussian filtering based edge-enhancement together with phase and ESTV projections. 28

3.5 DAPI stained cell nuclei image (100X) from Huh7 cells obtained with best possible focus: x_f and (b) another image with slight out of focus x_g. The images x_f and x_g are combined to obtain (c) the deblurred image using Gaussian filtering based edge-enhancement together with phase and ESTV projections. 29

3.6 The Huh7 cells nucleus image (100x) obtained with best possible focus: x_f and (b) another image with slight out of focus x_g. The images x_f and x_g are combined to obtain (c) the deblurred image using Gaussian filtering based edge-enhancement together with phase and ESTV projections. 30

3.7 Immuno-fluorescense images of CD133 positive Huh7 liver cancer cells with differential focus: (a) x_f (top), (b) x_g (middle). The images x_f and x_g are combined to obtain (c) the deblurred image using Gaussian filtering based edge-enhancement together with phase and ESTV projections. 33

3.8 Sample fluorescent labeled mouse liver tissue images used in experiments (a) Im-1, (b) Im-2 (c) Im-3, and (d) Im-4 obtained from [2]. 34

3.9 Sample deblurring results for "im-7": (a) Original image, (b) blurred image (Gaussian $\sigma = 5$); PSNR = 35.03 dB, (c) Image obtained by Ayers-Dainty with Phase and ESTV sets; PSNR = 40.24 dB, (d) Ayers-Dainty method; PSNR = 38.76 dB, (e) image obtained using [3]; PSNR = 32.32 dB. The blurring filter estimate for each case is shown in the bottom right corner. 35

4.1 (a) Two-dimensional (2D) point spread function (PSF) of MPI. The corresponding transfer function is a zero-phase function. (b) The real part of the transfer function is positive-valued, and (c) the imaginary part is completely zero (here (b) and (c) are displayed with identical windowing). 38

4.2 (a) The observed blurred MPI image, (b) its extended version, and (c) the support that marks the nonzero region used in spatial domain projections. Here, the spatial support is the same size as the imaging FOV, which is a very conservative estimate of the actual support of the MPI image. 41

4.3 (a) The original vein phantom, (b) the observed MPI image assuming blurring due to an SPIO size of 25nm, but no acquisition noise (PSNR = 14.66dB with respect to the vein phantom). The results of (c) Wiener deconvolution (PSNR = 28.38dB), (d) Lucy-Richardson deconvolution (PSNR = 26.14dB), and (e) the proposed algorithm (PSNR = 32.26dB) after 100 iterations. . . . 47

4.4 PSNR measured between the deconvolved image and the vein phantom (shown in Figure 4.3). Measurements are plotted as a function of the number of iterations for the Lucy-Richardson deconvolution and the proposed algorithm. Wiener deconvolution is displayed at a constant value, as it is a one-step algorithm. In this case, the proposed algorithm converges to a stable solution within 40 iterations, at significantly higher PSNR levels when compared to the other two methods. 48

4.5 MPI images of a vessel phantom with stenosis in a vertically oriented vessel. The vessel phantom (left column). The reconstructed x-space MPI images at varying noise levels, with direct feedthrough filtering (top row). The deblurred images with the proposed blind deconvolution method (bottom row). From left to right: No noise, and 40dB, 25db and 10dB MPI signal SNR. A zoomed-in portion near the stenosis region is shown in small display windows at the corner of each image. 49

4.6 MPI images of a vessel phantom with stenosis in a horizontally oriented vessel. The vessel phantom (left column). The reconstructed x-space MPI images at varying noise levels, with direct feedthrough filtering and nanoparticle relaxation effects (top row). The deblurred images with the proposed blind deconvolution method (bottom row). From left to right: No noise, and 40dB, 25db and 10dB MPI signal SNR. A zoomed-in portion near the stenosis region is shown in small display windows at the corner of each image. 53

4.7 PSNR measurements were performed between the deconvolved images and phantoms, and between the x-space reconstructed images before recovery and phantoms. Deconvolution was performed separately via the Wiener, Lucy-Richardson methods, and the proposed algorithm. (a) Measurements as a function of the MPI signal SNR level for direct feedthrough filtered case. (b) Measurements as a function of the MPI signal SNR level for direct feedthrough filtered case that also incorporates nanoparticle relaxation effects. 54

5.1 Flow-chart of the proposed Fourier phase and TV reduction based algorithm. 61

5.2 (a) A 60×60 non-symmetrical filter used in this study. (b) The real part and (c) imaginary part of 256×256 point DFT of this filter shows that the Fourier domain phases are non-zero. The dynamic range of (b) and (c) are normalized to display the DFT. 62

5.3 (a) Cropped version of the image "image_0111.jpg" from the database in [4] and (b) the blurred version of this image with noise ($\sigma = 1.5e-4$). The blurring filter is shown on top left corner of (b). The range of the image pixels intensities is [0, 1]. 62

5.4 Various filters used in deconvolution studies: (a) filter1, (b) filter2, (c) filter3 and (d) filter4 used in the tests. The size of the images are 60×60. 63

5.5 (a) A cropped portion of "image_0112.jpg". In the following four rows, images on the left are blurred versions of (a) with the PSF shown on top left corners and additive Gaussian noise with σ values: (b) 5×10^{-5}, (e) 7.5×10^{-5}, (h) 10^{-4} and (k) 1.5×10^{-4} (PSNR). The column in the middle are the results of Wiener deconvolution and the column on the right are the results of the proposed method. 67

5.6 (a) A cropped portion of "image_0119.jpg". In the following four rows, images on the left are blurred versions of (a) with the PSF shown on top left corners and additive Gaussian noise with σ values: (b) 5×10^{-5}, (e) 7.5×10^{-5}, (h) 10^{-4} and (k) 1.5×10^{-4} (PSNR). The column in the middle are the results of Wiener deconvolution and the column on the right are the results of the proposed method. 68

5.7 (a) A cropped portion of "image_0121.jpg". In the following four rows, images on the left are blurred versions of (a) with the PSF shown on top left corners and additive Gaussian noise with σ values: (b) 5×10^{-5}, (e) 7.5×10^{-5}, (h) 10^{-4} and (k) 1.5×10^{-4} (PSNR). The column in the middle are the results of Wiener deconvolution and the column on the right are the results of the proposed method. 69

5.8 (a) A cropped portion of "image_0124.jpg". In the following four rows, images on the left are blurred versions of (a) with the PSF shown on top left corners and additive Gaussian noise with σ values: (b) 5×10^{-5}, (e) 7.5×10^{-5}, (h) 10^{-4} and (k) 1.5×10^{-4} (PSNR). The column in the middle are the results of Wiener deconvolution and the column on the right are the results of the proposed method. 70

5.9 Comparison of PSNR convergence rates of four selected images versus the number of iterations. 71

List of Tables

3.1 Deconvolution results for FL microscopic images blurred by a Gaussian filter with disc size 20 and $\sigma = 5$. PSNR (dB) values are reported. 32

5.1 PSNR Results of the deconvolution of proposed method and Wiener deconvolution methods on blurred images with "filter1". 64
5.2 PSNR Results of the deconvolution of proposed method and Wiener deconvolution methods on blurred images with "filter2". 64
5.3 PSNR Results of the deconvolution of proposed method and Wiener deconvolution methods on blurred images with "filter3". 65
5.4 PSNR Results of the deconvolution of proposed method and Wiener deconvolution methods on blurred images with "filter4". 65

Chapter 1

Introduction

An important area of research in image processing aims to increase the image quality by reducing the blurriness that is introduced during image acquisition. There are many sources of blur ranging from the hardware that captures the image to the motion of the camera. One particular reason for blurriness in image generation applications such as Magnetic Resonance Imaging (MRI) or Magnetic Particle Imaging (MPI) might be the missing knowledge of Fourier domain frequency components of the underlying original image. On the other hand, in microscopic imaging, the source of blurriness is the optical characteristics of the capturing device. In such cases, even though the capturing device is optimized to reduce optical difficulties such as chromatic or spherical aberrations, a faulty focus problem may generate undesirable results.

The process of reducing the effects of blur in images is called deconvolution. The name suggests that this process is the inverse of convolution which is used to model the natural blurring processes in real life applications. The convolution is a straightforward procedure. However most of the convolved images obtained from real life problems are not ideal. They are either cropped so that the information beyond boundaries that affects the observation are not available to us, or the noise acting on the observation reduces success rates of solutions to inverse problems.

A wide range of algorithms are developed to deconvolve blurry images, see e.g. [5, 6, 7, 8]. Many of such algorithms are proposed to enhance the quality of microscopy images [9, 10, 11] which are mostly affected by out-of-focus type blurs. Microscopy images are also vulnerable to interference caused corruptions. In microscopy imaging, the Point Spread Function (PSF) may not be always available to us therefore the blind deconvolution algorithms are utilized for the microscopy image restoration problems [12, 13, 14, 3]. Sparsity analysis and usage of sparse reconstruction algorithms are also applied in this field [15, 16, 17]. Spatial domain image regularization algorithms are exploited for de-noising purposes in image restoration applications. Total Variation (TV) based regularization method is part of many in deconvolution methods used in microscopy images [18, 19, 20].

We use Fourier transform phase information to reconstruct out of focus microscopy images. We assume that PSF is symmetrical around the origin. As a result the phase of the observed image should be the same as the original image. We developed a blind deconvolution algorithm based on this observation.

Another problem addressed in this thesis is the reconstruction of Magnetic Particle Images (MPI) which are highly blurry due to their acquisition method. The superparamagnetic iron oxide (SPIO) particles injected to a patient responds to the applied magnetic field which in turn gives an estimate of the SPIO density [21, 22, 23]. The particle size highly affects the field of view (FOV) and the resolution. Reducing FOV increases resolution and therefore there is a trade off that needs to be carefully studied for human related applications [24, 25, 26, 27, 28]. In larger FOV cases, where the resolution is sacrificed, the degradation in resolution can be formulated by a convolution with a widely spread PSF [29, 30]. The problem can be considered as a deconvolution issue and well-known deconvolution methods are previously used in restoration of MPI images [31, 32]. In this thesis we propose a standalone method that iteratively restores the blurry MPI image using Fourier phase information of the observed image and TV based regularization.

Wiener deconvolution is a well-known method that restores blurred images based on the knowledge of the PSF and the information of noise spectral density.

Wiener deconvolution is widely used in image reconstruction problems including the microscopy and MPI image restoration [33, 34, 35, 36, 37]. Wiener deconvolution is a computationally efficient method. It requires an inverse Discrete Fourier Transform (DFT) computation and division per DFT component. Usually, it is not possible to estimate the power spectral density of the noise, therefore the deconvolution method can be summarized as direct element wise-division of Fourier coefficients of the observed image and the blurring filter plus a constant. We developed a computationally efficient approach that estimates the Fourier transform phase and magnitudes separately. After this step, an inverse DFT computation produces the deconvolved image similar to the Wiener filter.

The rest of the thesis is organized as follows: In Chapter 2, we give the theory and methods that lead us to the proposed deconvolution methods. We focus on microscopic images first and present the related image restoration methods in Chapter 3. We then present a Fourier transform phase and bounded energy projections based deconvolution algorithm targeting image enhancement of MPI problems in Chapter 4. In Chapter 5, we present an iterative algorithm in order to recover images from convolution with known filters. We conclude this thesis in Chapter 6.

Chapter 2

Theory and Methods of the Phase-based Image Restoration

2.1 Fourier Transform Phase

We mainly use the Fourier Transform (FT) phase of the observed image and the blurring filter to restore images. We assume a linear-space invariant model. The filtering process is defined as follows:

$$y[n_1, n_2] = x[n_1, n_2] * h[n_1, n_2], \tag{2.1}$$

where $x[n_1, n_2], h[n_1, n_2], y[n_1, n_2]$ are the original two-dimensional (2D) image, blurring filter and the resulting blurry image, respectively. The operator $*$ represents the 2D convolution operation. The blurring filter $h[n_1, n_2]$ defines the spread of each point in the original image onto the observed image $y[n_1, n_2]$, therefore this filter is also commonly known as point-spread-function (PSF). In the absence of noise, convolution in spatial domain corresponds to multiplication in Fourier domain as follows:

$$Y(\omega_1, \omega_2) = X(\omega_1, \omega_2)H(\omega_1, \omega_2), \tag{2.2}$$

where $X(\omega_1, \omega_2)$, $H(\omega_1, \omega_2)$ and $Y(\omega_1, \omega_2)$ are the 2D DTFTs of $x[n_1, n_2]$, $h[n_1, n_2]$ and $y[n_1, n_2]$, respectively. This relation yields that if the FT phase of two of the DTFTs are known in Equation 2.2, then it is possible to obtain the third FT phase by subtraction because,

$$\angle Y(\omega_1, \omega_2) = \angle X(\omega_1, \omega_2) + \angle H(\omega_1, \omega_2) \tag{2.3}$$

Image construction from Fourier transform phase has been extensively studied in the past [38, 39, 40, 41]. These studies suggest that FT phase alone has an important contribution in forming the image. An example of this hypothesis is visualized in Figure 2.1.



(a) (b) (c)

Figure 2.1: (a) A noisy version of "Lena" image, (b) reconstruction of "Lena" from FT phase with unit magnitude only and (c) reconstruction of noisy "Lena" from FT phase with unit magnitude only.

From the above example, using the relation of the FT phase of the two DTFTs in Equation 2.2 (FT phase of both Y and H), we may find the FT phase of X, which can then be used as an additional input on recovery of $x[n_1, n_2]$. The proposed recovery algorithms are detailed in the next two chapters.

In regular deconvolution problems, $h[n_1, n_2]$ is known. Therefore, its FT phase is also known. In blind deconvolution problems, however, $h[n_1, n_2]$ is not known.

The main difficulty in estimating the FT phase of $x[n_1, n_2]$ is that the PSF $h[n_1, n_2]$ is not available to us in many cases. In some imaging applications it is possible to directly observe this property by investigating the filtering response of a single point known in the image. However, this requires the prior knowledge of the original image, such as whether a single isolated point exists or not. If it exists, its location must also be known.

In blind deconvolution problems we will assume that the PSF is symmetrical with respect to the origin. In microscopic images, the reason for blur is mostly failed focus. Since optical components are symmetrical the blur PSF is also symmetrical. Therefore our assumption is a valid one in some microscopic images. Non-symmetrical blurs such as motion blur which is observed in fast moving object images are not considered in this case. Another class of image formation process in which the PSF is symmetrical is Magnetic Particle Imaging (MPI). When the PSF is symmetrical around origin:

$$\angle H(\omega_1, \omega_2) = 0 \text{ or } \pm\pi \tag{2.4}$$

A real valued symmetrical PSF $h[n_1, n_2]$ with size N_1 and N_2 in respective dimensions is defined as follows:

$$h[n_1, n_2] = h[-n_1, -n_2] \tag{2.5}$$

The corresponding DTFT is given by,

$$H(\omega_1, \omega_2) = \sum_{n_1, n_2} h[n_1, n_2] e^{-j(\omega_1 n_1 + \omega_2 n_2)} \tag{2.6}$$

In 1D when $h[n] = h[-n]$, we have;

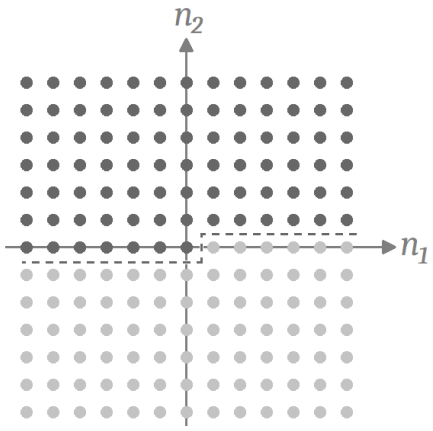


Figure 2.2: Upper half plane (UHP) indices are shown as dark points in (n_1, n_2) plane. The LHP is the bottom part.

$$\begin{aligned} H(\omega) &= h[0] + \sum_{n>0} h[n]e^{-j*\omega n} + \sum_{n<0} h[n]e^{-j*\omega n} \\ &= h[0] + 2\sum_{n} cos(\omega n) \end{aligned} \tag{2.7}$$

Therefore, $H(\omega)$ is real and its phase can be either zero or π when $H(\omega)$ is negative.

In 2D images, when we have half plane symmetry, we also have the "zero phase" case. Let the upper half plane be:

$$UHP = \{(n_1, n_2) | n_1 \leq 0 \text{ and } n_2 \geq 0, n_1 > 0 \text{ and } n_2 > 0\}, \tag{2.8}$$

as shown in Figure 2.2.

The lower half plane complements the upper half plane in the set of two dimensional integers. For half plane symmetry, it is expected the LHP to have identical values to the UHP as indicated by Equation 2.5. The DTFT of such a symmetrical image is then expressed as follows:

$$H(\omega_1, \omega_2) = \sum_{(n_1,n_2)\in UHP} h[n_1, n_2]e^{-j(\omega_1 n_1+\omega_2 n_2)} + \sum_{(n_1,n_2)\in LHP} h[n_1, n_2]e^{-j(\omega_1 n_1+\omega_2 n_2)} \tag{2.9}$$

or

$$\begin{aligned} H(\omega_1, \omega_2) = h[0, 0] + &\sum_{(n_1,n_2)\in UHP,\ (n_1,n_2)\neq 0} h[n_1, n_2]e^{-j(\omega_1 n_1+\omega_2 n_2)} \\ &+ \sum_{(n_1,n_2)\in LHP} h[n_1, n_2]e^{-j(\omega_1 n_1+\omega_2 n_2)} \end{aligned} \tag{2.10}$$

Whenever we can form cosines from complex exponentials, we can get real Fourier transforms. Using the symmetry property in Equation 2.5, we can rewrite the Equation 2.10 as follows:

$$H(\omega_1, \omega_2) = h[0, 0] + 2 \sum_{(n_1,n_2)\in LHP} h[n_1, n_2]cos(\omega_1 n_1 + \omega_2 n_2) \tag{2.11}$$

Therefore, the Fourier domain coefficients become real and their phases become either 0 or π.

Furthermore as the spread of the PSF decreases (Filter becomes all-pass), the Fourier domain coefficients also tend to be non-negative. In Fourier domain, the phase of the blurry image is equivalent to the sum of the PSF and the original image as a result of Equation 2.2. A PSF with all real and non-negative frequency components have zero phase in Fourier domain which results in the following relation:

$$\angle Y(\omega_1, \omega_2) = \angle X(\omega_1, \omega_2) \tag{2.12}$$

For large PSF, it may not always be possible to assume non-negative property of the symmetrical PSF, however in non-random signals, the lower frequency Fourier components have more contribution to the image than higher frequencies. For filters with narrow pass band around origin, Equation 2.12 still holds for lower frequency components which may be sufficient for recovery.

An example symmetrical filter with all real and non-negative FT components is Gaussian filter. In one dimension, the phase equality property of the Gaussian filter is visualized in Fig. 2.3. Even though it has negative Fourier components in high frequencies, disk shape filters with relatively small radius can be considered as zero phase when used for filtering natural images with small high frequency components.

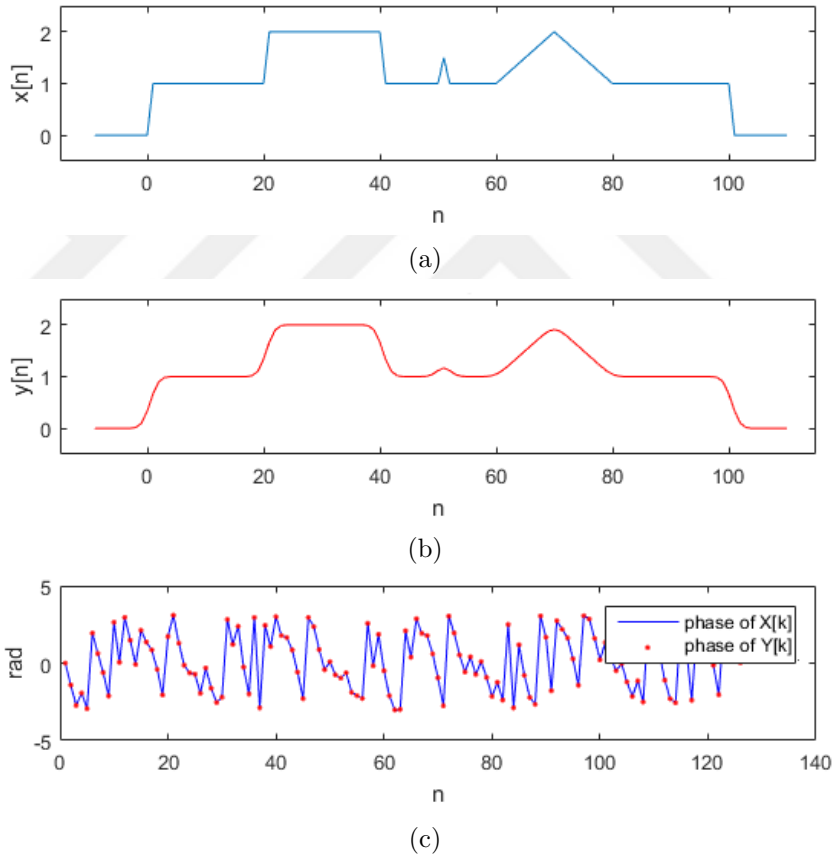


Figure 2.3: (a) The signal x is a 1D signal, (b) y is the filtered version of x with a Gaussian PSF with $\sigma = 1.2$ and, (c) Discrete Fourier Transform (DFT) phase of x and y for a DFT size of 130.

2.2 Energy Based Regularization Methods

We used FT phase as a constraint in Fourier domain. For spatial domain we need energy based constraints as regulators. This thesis presents two distinct

energy based approach for regularization in spatial domain. In Section 2.2.1, we present a Total Variation (TV) reduction based approach similar to the Epigraph Set of Total Variation (ESTV) projection that is used in [42]. In Section 2.2.2, regularization through ℓ_1 ball projection based approach is presented [43].

2.2.1 Total Variation Reduction

Total Variation (TV) in image processing represents the total amount of change of pixel values with respect to the neighboring pixels. A bound is defined over TV in many image denoising applications [44, 45, 46, 47, 48, 49]. In [42], the TV bound is used as a spatial domain regulator for deconvolution iterations. The TV of a 2D image is defined as follows:

$$\mathrm{TV}(x) = \sum_{k=0}^{N_1-2} \sum_{m=0}^{N_2-1} |x[k+1,m]-x[k,m]| + \sum_{k=0}^{N_1-1} \sum_{m=0}^{N_2-2} |x[k,m+1]-x[k,m]| \quad (2.13)$$

The set of images with the TV value less than a given ϵ is shown to be a closed and convex set [44]. A possible approach for reducing the TV of an image by manipulation of pixel values is through using the signs of the first derivative of the image as a normal vector of the TV set. That first derivative of the TV of image with respect to $x[n_1, n_2]$ given by:

$$\begin{aligned} d[n_1,n_2] = &\mathrm{sign}(x[n_1,n_2]-x[n_1+1,n_2])+ \\ &\mathrm{sign}(x[n_1,n_2]-x[n_1,n_2+1])+ \\ &\mathrm{sign}(x[n_1,n_2]-x[n_1-1,n_2])+ \\ &\mathrm{sign}(x[n_1,n_2]-x[n_1,n_2-1]) \end{aligned} \quad (2.14)$$

All the pixel values in x have a corresponding contribution to the TV defined in d. A gradient descent type algorithm can be obtained as follows; Let $x^{(i)}$ be the current iterate and $x^{(i+1)}$ the next iterate, then

$$x^{(i+1)}[n_1, n_2] = x^{(i)}[n_1, n_2] + \alpha d[n_1, n_2], \tag{2.15}$$

where α is a small coefficient that controls the amount of reduction in TV during the iterations. A large α value may result in over reduction (or increments) in pixel values that actually starts to increase the TV of the image. Hence, a small α with multiple iterations are preferable.

The iteration procedure defined in Equation 2.15 is not a true projection. However, a projection onto the set of images with zero TV will be obtained without a constraint. Fourier domain phase set provides this constraint on TV and we only carry out a single pass on pixels of the image for $n_1 = 0, 1, ...N-1$, $n_2 = 0, 1, ...N-1$ respectively. In Section 2.3.2, a different approach for reduction of TV is presented.

2.2.2 Projections onto ℓ_1 Ball

In this thesis, we also utilized an ℓ_1 ball projection based regularization algorithm in spatial domain. The ℓ_1 norm based regularization is applied by projection onto the close and convex set S_1^ϵ based on ℓ_1 norm [48]:

$$S_1^\epsilon = \{x \mid ||x||_1 \leq \epsilon\} \tag{2.16}$$

where ϵ is a predetermined upper bound, and,

$$||x||_1 = \sum_{n_1,n_2} |x[n_1, n_2]|. \tag{2.17}$$

This regularization can be implemented through an orthogonal projection onto S_1^ϵ [50, 51, 52]. It is also possible to select the upper bound ϵ in an adaptive manner using the epigraph set concept described in [42]. We present an approximate projection operator to speed up the iteration process. The magnitudes of the result of the projection is independent of the signs, therefore it is possible to consider the absolute values of the pixels and incorporate the original signs later.

As a result, we consider only the first 'quadrant' of the ℓ_1 ball as shown in Figure 2.4.

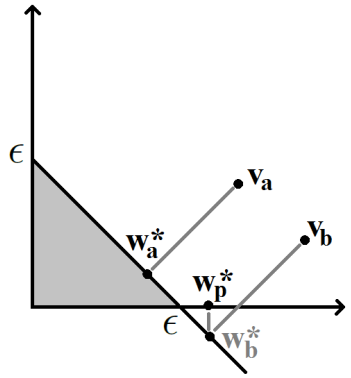


Figure 2.4: Shaded area represents the first quadrant of the 2D version of ℓ_1 ball. The vector $\mathbf{w_a^*}$ is the projection of $\mathbf{v_a}$ onto the ℓ_1 ball. The projection of $\mathbf{v_b}$ is difficult to compute in high dimensions, but $\mathbf{w_p^*}$ can be used instead of the projection.

Let $\mathbf{v_a}$ be the vectorized version of the current iterate $x^{(i)}$ image, i.e., $\mathbf{v_a}[k] = x^{(i)}[n_1, n_2]$ for $k = n_1 + n_2 N_1$. In Figure 2.4, $\mathbf{w_a^*}$ is the orthogonal projection of $\mathbf{v_a}$ onto the ℓ_1 ball. The vector $\mathbf{w_a^*}$ is the solution of the following problem:

$$\mathbf{w_a^*} = \text{argmin}||\mathbf{v_a} - \mathbf{w}||_2^2 \; \textit{such that} \; \sum_{i=0}^{N-1} |w[i]| \leq \epsilon \tag{2.18}$$

where $N = N_1 \cdot N_2$ is the total number of pixels in the image $x^{(i)}$. In case $\mathbf{v_a}$ lies inside the shaded area, the minimizing point w_a^* is equal to v_a, however if the point is outside the shaded area, the following operation is defined:

Because we only consider the all-positive part of the ℓ_1 ball, the solution can be found by minimizing the Lagrangian.

$$\mathcal{L} = \frac{1}{2}||\mathbf{w} - \mathbf{v_a}||^2 + \lambda \left(\sum_{i=0}^{N-1} w[i] - \epsilon \right) \tag{2.19}$$

where $\sum_{i=0}^{N-1} w[i] = \epsilon$ is the hyperplane determining boundary of the ℓ_1 ball.

By computing the partial derivatives with respect to the entries of unknown vector $\mathbf{w}$ and the Lagrange multiplier λ, we can determine the projection of $\mathbf{v_a}$

onto the hyperplane $\sum_{i=0}^{N-1} w[i] = \epsilon$ as follows:

$$w[i] = v_a[i] - \lambda \tag{2.20}$$

and

$$\lambda = \frac{1}{N}\left(\sum_{i=0}^{N-1} v_a[i] - \epsilon\right) \tag{2.21}$$

Therefore, the vector $\mathbf{w_a^*}$ is given by

$$w_a^*[i] = v_a[i] - \frac{1}{N}\left(\sum_{i=0}^{N-1} v_a[i] - \epsilon\right) \tag{2.22}$$

The vector $\mathbf{w_a^*}$ may or may not be the orthogonal projection onto the ℓ_1 ball as shown in Figure 2.4. If all the entries $w_{a,i}$ of $\mathbf{w_a^*}$ are non-negative, it is the projection vector. However, some of the entries of the projection vector $\mathbf{w_b^*}$ corresponding to $\mathbf{v_b}$ may become negative as shown in Figure 2.4. In this case we zero out the negative entries of $\mathbf{w_b^*}$ and obtain $\mathbf{w_p^*}$ as shown in Figure 2.4:

$$w_p^*[i] = \begin{cases} w_b^*[i], & if\ w_b^*[i] \geq 0 \\ 0, & if\ w_b^*[i] < 0 \end{cases} \tag{2.23}$$

Although the vector $\mathbf{w_p}$ can be further processed to determine the projection vector onto the ℓ_1 ball, we use $\mathbf{w_p^*}$ in our algorithm. This speeds up the iteration process compared to the exact ℓ_1 projection, because exact ℓ_1 projection requires sorting all the elements of a given image [53]. By using $\mathbf{w_p^*}$, we eliminate the sorting process.

The goal of projection onto ℓ_1 ball is to zero out small valued coefficients of the vector $\mathbf{v_b}$. This goal is achieved by Equation 2.23. The signal $\mathbf{w_p}$ is "sparse" version of $\mathbf{v_b}$.

Equation (2.23) is very useful during iterations, because it not only removes noise but also suppresses small image coefficients, enforcing the image energy to be concentrated on stronger coefficients.

2.3 Projection onto Convex Sets (POCS)

Projection onto Convex Sets (POCS) method aims to find a solution to problems, in which, the solution is known to belong to the intersection of a number of closed and convex sets [54, 55, 56, 50]. It is widely used in many image processing applications, where multiple image features can be associated with multiple closed and convex sets [57, 58, 59, 60, 61, 62, 63, 64, 65, 66]. The method relies on iterative projections onto the convex sets until a valid solution which satisfies all the conditions are found or a predetermined number of iterations are executed. This limit is set for the cases where the convex sets are disjoint and no solution to satisfy all convex sets exist. In that case solution is found to satisfy at least one of the convex sets depending on where the iterations are stopped.

Another issue may occur if the intersection of convex sets is not unique. In this case there are more than one solution to the POCS problem and the final result depends on the initial conditions. We describe the utilized convex sets for deconvolution.

2.3.1 Projection onto the Phase Set

We define the following set of images with known Fourier transform phase:

$$S_\Phi = \{x[n_1, n_2] | \angle X(\omega_1, \omega_2) = \Phi(\omega_1, \omega_2)\}, \tag{2.24}$$

where $\Phi(\omega_1, \omega_2)$ is the phase of $x[n_1, n_2] \in S_\Phi$. Let $v[n_1, n_2]$ be an arbitrary signal with DTFT, $V(\omega_1, \omega_2) = |V(\omega_1, \omega_2)|e^{j\angle V(\omega_1, \omega_2)}$. The projection $V_p(\omega_1, \omega_2)$ of $V(\omega_1, \omega_2)$ onto the set S_Φ is given by:

$$V_p(\omega_1, \omega_2) = |V(\omega_1, \omega_2)|e^{j\Phi(\omega_1, \omega_2)} \tag{2.25}$$

The projection is defined in a straight-forward way. However, in order to use

this projection in POCS method, we first need to prove the convexity of the set S_Φ.

2.3.1.1 Convexity of Phase Set

For two images V_{p1} and V_{p2}, if they both are in the set S_Φ, then they satisfy the condition given in Equation 2.25. Any point V_m on the line in between these two solutions in the solution space can be defined as follows:

$$V_m(\omega_1, \omega_2) = \beta V_{p1}(\omega_1, \omega_2) + (1-\beta)V_{p2}(\omega_1, \omega_2), \quad 0 \leq \beta \leq 1 \tag{2.26}$$

We can rewrite this equation using Equation 2.25:

$$V_m(\omega_1, \omega_2) = (\beta V_1(\omega_1, \omega_2) + (1-\beta)V_2(\omega_1, \omega_2))e^{j\Phi(\omega_1,\omega_2)}, \quad 0 \leq \beta \leq 1 \tag{2.27}$$

The phase of V_m is then $\Phi(\omega_1, \omega_2)$. Therefore it is shown that $V_m \in S_\Phi$. This proves the convex property of the phase set S_Φ. Since Fourier and inverse Fourier transformations are linear operations, we conclude that the phase set S_Φ and its counterpart in spatial domain are both convex.

Once the projection onto S_Φ is performed, spatial domain signal $v_p[n_1, n_2]$ can be computed using the inverse FT of $V_p(\omega_1, \omega_2)$.

2.3.2 Approximate Projection onto TV Set

In Section 2.2.1, we introduced the TV concept and presented a method to reduce TV of an image. In this section, we present an approximate TV reduction algorithm that can be utilized in POCS method.

We can perform the approximate projection operation in three steps. We first high-pass filter the image x and then project the high-pass filtered image x_h onto ℓ_1 ball. In the last step we combine the output of ℓ_1 projection with the low-pass filtered version of x.
Let,

$$x = x_{lp} + x_{hp} \tag{2.28}$$

where x_{lp} is the low-pass and x_{hp} is the high pass components of x. The image x_{hp} can be obtained using the Haar filter or any other high-pass filter. This decomposition is easy to obtain as follows:

$$x_{hp} = x - h_{lp} * x \tag{2.29}$$

where h_{lp} is an approximate low-pass filter. The image is the ℓ_1-projected version of x_{hp}:

$$x_{1hp} = P_1(x_{hp}) \tag{2.30}$$

This projection can be also approximated by Equation 2.23. After this step we obtain the approximate total variation reduced image x_{ATV} as follows:

$$x_{ATV} = x_{lp} + x_{1hp} \tag{2.31}$$

which approximates projection onto the TV set. The main motivation is that x_{hp} is a sparse image mainly containing edges and noise of the original image. Projection onto the ℓ_1 ball removes noise and the remaining part contributes to the image $x_{A.TV}$.

The advantage of this method to the more accurate TV reduction defined in section 2.2.1 is that this method is composed of simple convolution operations. It is easier to compute and faster to execute.

2.3.3 Comparison Measure

We make comparisons on the success rates of the presented algorithms with the results of the well-known methods such as Wiener and Ayers-Dainty deconvolution algorithms. The respective algorithms available in MATLAB are used in comparison [67]. Our success measure is Peak-Signal to Noise Ratio defined as:

$$PSNR = 10\log_{10}\left(\frac{MAX^2}{MSE}\right) \tag{2.32}$$

where, MAX is the peak signal intensity of the ideal image and the MSE is the root-mean-squared error between the ideal and the deconvolved image. PSNR is evaluated in dB. The main advantage of PSNR to SNR is that the similarity in results of different intensity levels. SNR has a tendency to give better results in bright images where the dark images show low SNR if the noise is not dependent on image intensity. PSNR prevents the issue giving similar results for all intensities.

2.4 Summary

We described the theoretical background that lead us to Fourier phase based deconvolution algorithms. We have shown that the half plane symmetrical filters result in real Fourier transform coefficients. Furthermore the spread of the PSF highly affects the size of the region where we observe non-negative Fourier transform coefficients, creating a similarity between the Fourier phase of the original and the observed image.

We also presented TV reduction and ℓ_1 ball projection based spatial domain regularization methods. These spatial domain constraints are used in iterative algorithms. The ideas presented here are used in the following chapters for use in microscopy and MPI images. The more general non-blind deconvolution algorithm presented in Chapter 5 also utilizes the TV reduction based regularization presented here.

Chapter 3

Fourier Transform Phase and Total Variation Based Improvement of Blind Deconvolution Methods

We applied the concepts described in Chapter 2 on existing Ayers-Dainty blind deconvolution technique [68]. We then test the concept through experiments on microbiology images. This chapter is organized as follows: in Section 3.1, we introduce the problem and summarize previous works on microscopic image enhancement. In Section 3.2, we present the phase and TV based convex sets and in Section 3.3, we show the incorporation of above mentioned sets onto well known Ayers-Dainty blind deconvolution process through POCS method. We present experimental results in Section 3.4 and summarize our work in Section 3.5.

3.1 Previous Studies in Image Quality Enhancement of Microbiology Images

Blind deconvolution is a well-studied subject in image processing. Unlike the non-blind techniques, blind deconvolution is required in cases where the PSF is not available to us. Microbiology images are good examples of such cases where the PSF depends on many variables such as the shape of aperture or focal length of the optical image acquisition apparatus.

In [9], a statistical approach is pursued in order to enhance Signal to Noise Ratio (SNR) on 4D fluorescence microscopic images. Chan and Wong [18] uses TV for regularization. In [19, 20], well-known Richardson-Lucy blind deconvolution technique is improved with reduced TV in order to reduce the degradation on microscopic images caused by out of focus light and Poisson noise. Zhang et al. [11] aims to model the PSF of fluorescence microscope PSF. In doing this, they specifically focus on three different image acquisition methods; wide field fluorescence microscope (WFFM), the laser scanning confocal microscope (LSCM), and the disk scanning confocal microscope (DSCM) and obtain the Gaussian parameters of the optical characteristic models of these microscopes.

Deconvolution methods non-specific to microscopy images can also be utilized for microscopy image recovery [5, 6]. Xu et al. [15] and Ye et al. [16] focus on $L0$ sparse representation for restoration of motion blurred images. Bostan et al. [17] proposes a maximum a posteriori (MAP) estimator in order to solve ill-posed linear inverse problems.

We present the well-known Ayers-Dainty blind deconvolution algorithm [68], utilized as the basis for deconvolution of microscopic images. In spatial domain, we also exploit TV property of the image in order to reduce noise.

3.2 Convex Sets Used in Blind Deconvolution

The POCS theorem is discussed in detail in Section 2.3. For the microscopy imaging blur issue, the proposed convex sets are determined to be the set of images with known FT phase and the set of images with a bounded TV as described in Sections 2.1 and 2.2.1.

3.2.1 Extraction of Fourier Transform Phase

The optical symmetry of the image acquisition apparatus in microbiology images results in symmetrical filters. From the properties of symmetrical PSF discussed earlier, we may assume that the FT phase of the blurred image represents high similarities to the FT phase of the underlying original image. The first step is to extract phase information from the blurry image. However, the FT phase extraction process comes with difficulties due to cropped nature of microscopy images.

For a given 2D image x and 2D PSF h, the blurry image is modelled by the following 2D discrete operation:

$$y[n_1, n_2] = \sum_{k=-\infty}^{\infty} \sum_{k=-\infty}^{\infty} x[k, m] h[n_1 - k, n_2 - m] \tag{3.1}$$

The image index values n_1 and n_2 range from 0 to N_{y1} and 0 to N_{y2} respectively. We also assume that h to be a finite extend impulse response (FIR) filter and the size of h is also limited. In order to extract the FT phase from y and match these values with the FT phase of x, we need the complete size of the observed image y. From Equation 3.1, we observe that the value of y depends on the the pixel values of x beyond the limits of $[0, N_{y1}]$ and $[0, N_{y2}]$. Furthermore spread of some of the pixel values of x may reach out of the borders of observed image y. Therefore, we have an ill-posed linear inverse problem.

In our algorithm, we try to reduce the effects of the secondary issue of pixels spreading beyond borders by gradually decreasing the values of the border pixels to zero. In this way the estimate effects of a framed and extended x are simulated on y. We call this frame as 'support'.

The introduction of a support in spatial domain also gives us an additional spatial domain constraint. In every iteration we zero out the pixel values that are outside the range of the support. This finite support set is also a closed and convex set and it is used in many image restoration problems [69, 70, 38].

The estimation by gradual decrease of borders introduces a high noise into the observed image. We also assume that the noise is independent of our operations that is naturally available as in every image processing applications. The observed image with this observation noise becomes:

$$\tilde{y} = y + n \tag{3.2}$$

where n is the additive noise. In this case, the FT phase of the observed image is definitely different from the FT phase of the original image. However the noise robustness of phase information is experimentally observed by many researchers as shown in Chapter 2 [38]. Therefore an estimate of phase from noisy image is still usable in practical applications.

After the gradual decrease process, the phase of the newly generated $\hat{y}$ is assumed to be equal to the phase of support added image $\hat{x}$ considering the PSF is non-negative and real in all frequencies. If more knowledge on the nature of the PSF is available, it is possible to estimate the negative transitions of FT phase of the PSF. In that case the phase of the observed image $\hat{Y}(\omega_1, \omega_2)$ differs from the original image $\hat{X}(\omega_1, \omega_2)$ by π. Then the phase transition from $\hat{Y}$ to $\hat{X}$ must be corrected taking the phase jump into account by phase unwrapping algorithms. We take zero phase property of PSF for granted since the technique is blind and we have no knowledge on PSF except that it is originated by an optical process which is known to be symmetrical with respect to the origin.

3.2.2 Spatial Domain Sets

As a continuation of the POCS based approach we can formulate the spatial domain constraints as closed and convex sets. The closed and convex nature of bounded TV set is described previously. We introduce two additional convex sets which are crucial for a successful image recovery.

The first added set is the spatial support discussed in the previous Section. The support is defined to be the region where the original pixel values of the observed image resides (The extended portion of the image is excluded). Let s_f be the support region in the spatial domain. Then the related set of images is defined as:

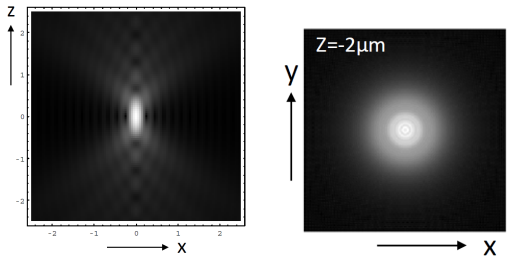
$$S_s = \{x | x[n_1, n_2] = 0, \quad [n_1, n_2] \notin s_f\} \tag{3.3}$$

The projection onto S_s is also simple:

$$x_s[n_1, n_2] = \begin{cases} x[n_1, n_2], & if\ [n_1, n_2] \in s_f \\ 0, & otherwise \end{cases} \tag{3.4}$$

where x_s is the projection of iterate x onto the support set S_s.

The final spatial domain constraint used in this study is the positivity set. The origins of this set is straightforward. The PSF of optical components are non-negative, meaning that the pixel values of the original image cannot have a negative contribution on the observed image. Even though the wave property of light may cause deletion of light (due to interference), this is not the reason for degradation in practical optical measurements. Therefore the modelled PSF is observed to have non-negative real values. The original image must also have a similar property. The pixel values typically start from 0 in the darkest regions of the images. Therefore, the blurred image is also expected to have the same property.



(a) (b)

Figure 3.1: Examples of microscopy imaging PSFs (a) in multiple focus levels and (b) in a single out-of-focus distance ($2\mu m$). In (b) an interference related symmetrical pattern is visible which yields real Fourier domain components. [Image courtesy of Pascal Chartrand, University of Montreal.]

We can use this property as a projection onto the set S_{pos}:

$$S_{pos} = \{x | x[n_1, n_2] \geq 0\}, \tag{3.5}$$

which is a closed and convex set in ℓ_2 [70]. The projection onto S_{pos} is performed as follows:

$$x_{pos}[n_1, n_2] = \begin{cases} x[n_1, n_2], & if\ x[n_1, n_2] \geq 0 \\ 0, & otherwise \end{cases} \tag{3.6}$$

The defined three closed and convex sets are used as spatial domain constraint in order to regulate iterates. Apart from these, a symmetry constraint is applied on the PSF iterates; the filter is updated to be symmetrical in every iteration since this was one of the main assumptions of microscopy image recovery.

3.3 Improved Ayers-Dainty Blind Deconvolution Techniques using POCS Method

In this section, we present an algorithm that integrates FT phase, spatial domain support and TV reduction based features onto blind Ayers-Dainty deconvolution

method.

Ayers-Dainty is one of the earliest blind deconvolution methods that iterates between spatial and Fourier domain. The algorithm starts with a preparation process in which the borders are gradually decremented as explained in Section 3.2.1. This procedure defines a support that will be used among spatial domain constraints. Iterations start with an initial guess $x_0[n_1, n_2]$. The method successively updates the PSF $h_(i)[n_1, n_2]$ and $x_{(i)}[n_1, n_2]$ at the ith iteration as follows:

1. Compute $\hat{X}_i(\omega_1, \omega_2) = \mathcal{F}\{\hat{x}_i[n_1, n_2]\}$, where $\mathcal{F}$ represents the 2D DTFT operation.

2. Estimate the blurring filter response using the following equation

$$\tilde{H}_i(\omega_1, \omega_2) = \frac{Y(\omega_1, \omega_2)\hat{X}_i^*(\omega_1, \omega_2)}{|\hat{X}_i(\omega_1, \omega_2)|^2 + \alpha/|\hat{H}_i(\omega_1, \omega_2)|^2}, \tag{3.7}$$

   where α is a small real number.

3. Compute the inverse DTFT $\tilde{h}_i[n_1, n_2] = \mathcal{F}^{-1}\{\tilde{H}_i(\omega_1, \omega_2)\}$ to estimate a filter response.

4. Impose the positivity constraint and support constraints on $\tilde{h}_i[n_1, n_2]$. Let the output of this step be $\hat{h}_i[n_1, n_2]$.

5. Compute $\hat{H}_i(\omega_1, \omega_2) = \mathcal{F}\{\hat{h}_i[n_1, n_2]\}$.

6. Update the image

$$\tilde{X}_i(\omega_1, \omega_2) = \frac{Y(\omega_1, \omega_2)\hat{H}_i^*(\omega_1, \omega_2)}{|\hat{H}_i(\omega_1, \omega_2)|^2 + \alpha/|\hat{X}_i(\omega_1, \omega_2)|^2}. \tag{3.8}$$

7. Compute $\hat{x}_i[n_1, n_2] = \mathcal{F}^{-1}\{\hat{X}_i(\omega_1, \omega_2)\}$.

8. Impose spatial domain positivity and finite support constraint on $\hat{x}_i[n_1, n_2]$ to produce the next iterate $\hat{x}_{i+1}[n_1, n_2]$.

We stop the iterations under two conditions: (i) whenever there is no significant change between successive iterates or (ii) whenever a predetermined number of iterations are executed.

In the above algorithm, the phase information can be imposed on the current iterate as follows:

$$\bar{X}_i(\omega_1, \omega_2) = |\check{X}_i(\omega_1, \omega_2)| e^{j\angle Y(\omega_1, \omega_2)}, \tag{3.9}$$

where $\angle Y(\omega_1, \omega_2)$ is the phase of $Y(\omega_1, \omega_2)$.

The step 7) is modified to $\bar{x}_i[n_1, n_2] = \mathcal{F}^{-1}\{\bar{X}_i(\omega_1, \omega_2)\}$.

The flowchart of the proposed algorithm is shown in Figure 3.2.

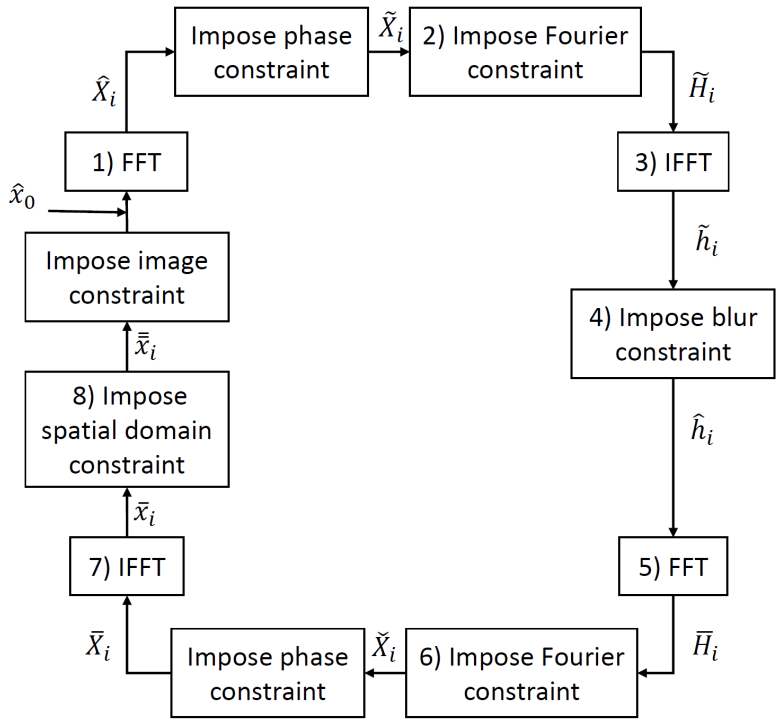


Figure 3.2: The flowchart of the improved Ayers-Dainty method.

Global convergence of Ayers-Dainty deconvolution has not been proven. Furthermore in our experiments, we observed divergence in some cases. The added projections do not introduce further divergence problems since projections onto

convex set is non-expansive operation [71, 72, 73]. It regularizes the iterative Ayers-Dainty method.

3.4 Experimental Results

In our experiments we used Peak-Signal to Noise Ratio quality measure. We tested the presented algorithm with the example in [1]. This online resource is linked by the EPFL 3D Deconvolution in microscopy webpage. In Figure 3.3 (a) the original image is shown. This image is filtered with a Gaussian PSF with $\sigma = 6$ which is given in 3.3(b). From (c) to (f) we compare the results of blind/non-blind deconvolution algorithms as well as the proposed technique. The PSNR values are also provided as accuracy measure. We see that the cable in the figure is visible in FT phase/spatial domain constraint extended Ayers-Dainty method. Some ringing artifacts are also visible.

3.4.1 Blind Deconvolution of 3D images

In this subsection we present 3D stack image deconvolution examples. Different layers of 3D stack fluorescent microscopy (FL) images can be used to obtain single deconvolved image with clear features. The goal of this section is to describe image reconstruction examples in FL images. Each layer has a different focus level. Therefore some portions of each image is out of focus. The proposed algorithm fuses these layer images and reconstructs a single image.

The images in Figure 3.4 (a) and (b) are obtained by the Nikon ECLIPSE Ti-S microscope. These are the images of Huh7, human hepatocellular carcinoma cells (ATCC), which were maintained in Dulbecco's Modified Eagle's Medium (DMEM) (Invitrogen GIBCO), supplemented with 10% fetal bovine serum (FBS) (Invitrogen GIBCO), 2 mM L-glutamine, 0.1 mM nonessential amino acids, 100 units/mL penicillin and 100 g/mL streptomycin at 37 °C in a humidified incubator under 5% CO_2. The first image is focussed as good as possible. The image in

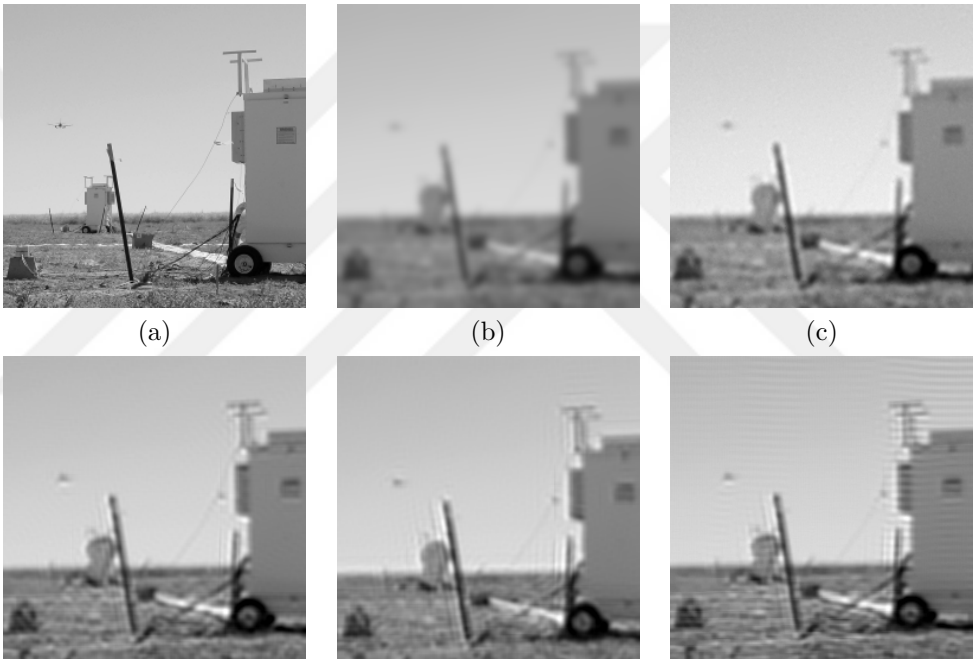


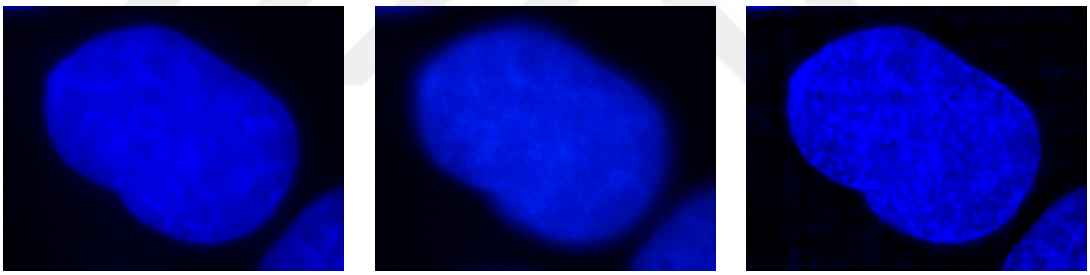
Figure 3.3: Comparison of deconvolution algorithms: (a) The test image from [1], (b) Observed image blurred by Gaussian filter with $\sigma = 6$. (c) Image deblurred by the non-blind deconvolution method in [1], PSNR = 22.43dB, (d) Image deconvolved by pure Ayers-Dainty method, PSNR = 24.86 dB. (e) Result of the presented phase projection based Ayers-Dainty extension, PSNR = 24.91 dB. (f) Results of Ayers-Dainty method with FT phase and spatial domain projections, PSNR = 25.18 dB.

Figure 3.4 (b) is slightly out of focus. In order to obtain the result shown in Figure 3.4(c) we used 3D edge enhancement algorithm together with FT phase and spatial domain projections.

The Gaussian filter based edge enhancement is achieved using the following equation:

$$x_e = x_f + c_h(x_g - h * x_g), \tag{3.10}$$

where h is a 2D Gaussian filter with $\sigma = 5$ and $c_h = 0.3$ is the high frequency component amplification coefficient. High frequency components of x_g is added onto the better focused image x_f. After this step the edge-enhanced image x_e is successively projected onto the phase and spatial domain sets in an iterative manner. The image shown in Figure 3.4(c) is obtained after 100 iterations.



(a) (b) (c)

Figure 3.4: (a) DAPI stained cell nuclei image (100X) from Huh7 cells with best possible focus: x_f and (b) another image with slight out of focus x_g. The images x_f and x_g are combined to obtain (c) the deblurred image using Gaussian filtering based edge-enhancement together with phase and ESTV projections.

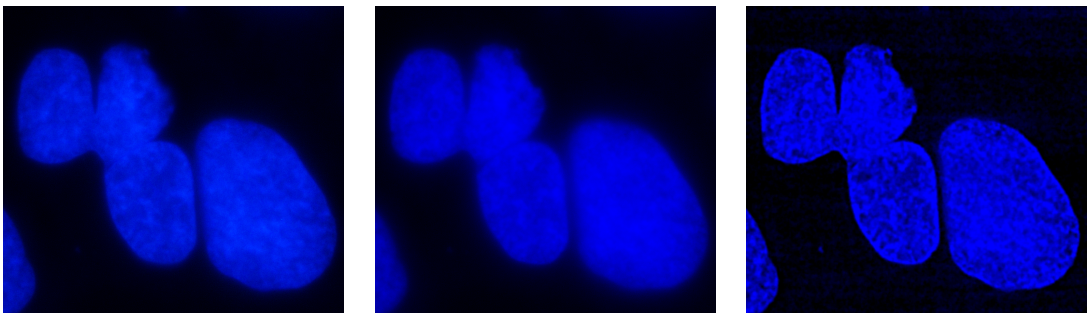
For the image in Figure 3.4 we do not have a ground-truth for PSNR calculation, however we can verify improvements visually. After around 100 iterations, the improvements are seen to stabilize.

Huh7 cells were stained using CD133 seeded onto coverslips (50000 cell/well) in 6-well plates and grown for 72 hours until cells reached 80% confluency. Cells were fixed with cold 4% paraformaldehyde for 30 min at room temperature and washed with 1xPBS. For blocking cells were incubated with 3% BSA-PBS-T(0.1%) for 90 minutes on a shaker at room temperature. Primary antibody incubation was

done using human anti-CD133/2 (MACS cat.# 130-090-851) for an hour as recommended by the manufacturer. Cells were washed 3 times with 1xPBS for 5 minutes. Secondary antibody incubation were done using Alexa-fluor 488 goat anti-mouse IgG antibody (Invitrogen cat.# A11029, 1:1000) for an hour. After repeating the washing step, counterstaining (DAPI) was done using UltraCruz Mounting Medium (Santa Cruz cat.# sc-24941).

Time-lapse images of fluorescently stained cells were taken using Nikon ECLIPSE Ti-S inverted microscopy and NIS-Elements Viewer software. Cell nuclei images shown in Figure 3.7 were taken using 340-380 nm filter (duration: 1 minute, interval: 1 sec) under 150 ms exposure. CD133 positive cell time-lapse images shown in Fig. 9 were taken using the 465-495 nm filter (duration: 1 minute, interval: 1 sec) under 600 ms exposure.

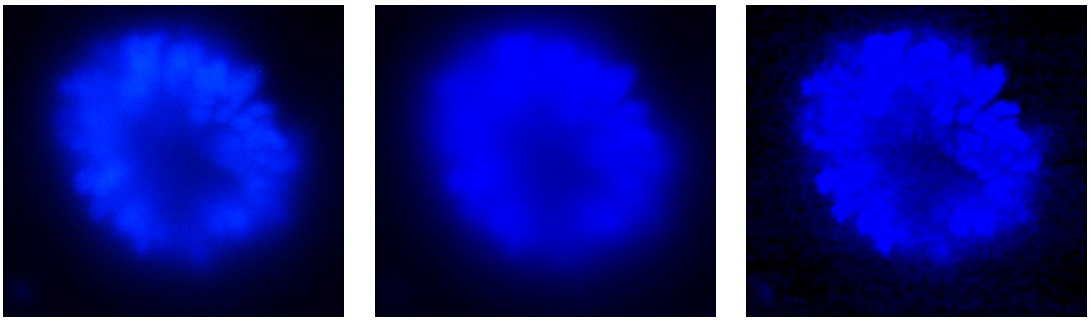
Other examples of microscopy image recovery are presented in Figures 3.5 and 3.6. It is clear that the phase information has improving effects of the quality of the results.



(a) (b) (c)

Figure 3.5: DAPI stained cell nuclei image (100X) from Huh7 cells obtained with best possible focus: x_f and (b) another image with slight out of focus x_g. The images x_f and x_g are combined to obtain (c) the deblurred image using Gaussian filtering based edge-enhancement together with phase and ESTV projections.

We also tested the presented algorithm with two immuno-fluorescence z-stack images of CD133 positive Huh7 liver cancer cells as shown in Figure 3.7. The images in (a) and (b) represents different focus levels of the same image. They are combined via Equation 3.10 with $\sigma = 10$ and $c_h = 0.3$. The resulting image



(a) (b) (c)

Figure 3.6: The Huh7 cells nucleus image (100x) obtained with best possible focus: x_f and (b) another image with slight out of focus x_g. The images x_f and x_g are combined to obtain (c) the deblurred image using Gaussian filtering based edge-enhancement together with phase and ESTV projections.

in Figure 3.7 (c) is obtained by 20 iterations of FT phase and spatial domain set projections.

3.4.2 2D Blind Deconvolution with Ayers-Dainty Method

We investigate the improvement of well known Ayers-Dainty method with the introduction of FT phase and spatial domain projections. The images tested in this Section are fluorescence (FL) microscopy images obtained at Bilkent University as a part of a project to track motility and migration of cells, funded by Turkish Scientific Research Council and German BMBF. The contact inhibition phenomena as a result of cell migration was first described in 1950s [74] in cultured cells which indicated that cell migration and motility are under the control of cell signaling. Cell migration and motility is a cellular activity that occurs during various stages of the life cycle of a cell under normal or pathological conditions. Embryonic development, wound-tissue healing, inflammation, angiogenesis, cancer metastasis are some of the major cellular activities that involve cell motility.

We use a video object tracker to track cells; however, due to low focal performance, the images were smooth and unusable. The blind deconvolution extension

is used in sharpening the edges for cell tracking purposes. The images that we used are single layered. Therefore the presented deconvolution is applied on a single image.

For evaluation of the presented method using PSNR as a success measure, we selected sharp cell images from fluorescent microscopy data set and synthetically blurred these using a 20×20 Gaussian filter with $\sigma = 5$. The results of already blurry images are also visually examined. The presented method is tested against blind Ayers-Dainty method. In all cases the initial estimate image was a single nonzero pixel image which prevented zero magnitudes in any frequency components. Furthermore we compared our method with another blind deconvolution method proposed in [3].

In Fig. 3.8, some sample images used in experimental studies are shown. Ayers-Dainty method is compared with its own extension using FT phase and ESTV sets.

The iterations for Ayers-Dainty and presented methods are limited to 300. Table 3.1 presents the results of the presented algorithm as well as the method presented in [3]. The latter method [3] has poor performance when compared to Ayers-Dainty related methods. Image deblurring results of a selected image (Labelled as im-7) is shown in Figure 3.9.

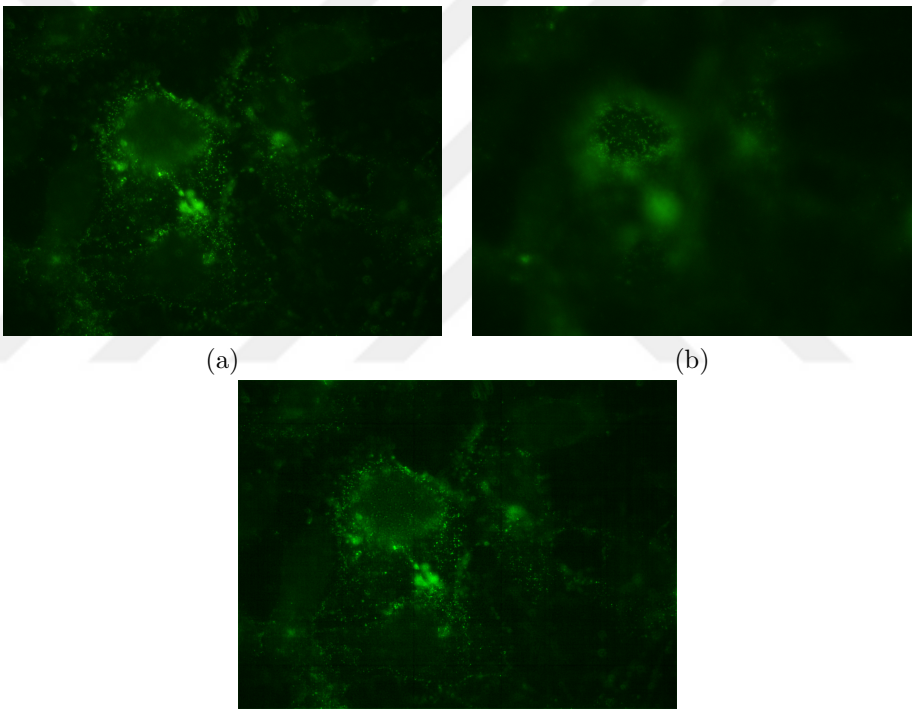
The performance results of presented algorithm compared to other algorithms is given in Table 3.1. bold PSNR values are the best results for a given image. We observed that the FT phase accompanied by spatial domain constraints gives the best results. The method described in [3] cannot improve fine details of FL images as shown in Figure 3.9 and Table 3.1. Four example images for which the results are given in this table are shown in Figure 3.8.

Table 3.1: Deconvolution results for FL microscopic images blurred by a Gaussian filter with disc size 20 and $\sigma = 5$. PSNR (dB) values are reported.

Image	Initial PSNR	Ayers-Dainty	Ayers-Dainty with Phase	Ayers Dainty Phase & Spatial Domain Constraints	Method in [3]
im-1	32.08	34.25	34.51	**35.19**	31.43
im-2	31.86	31.59	31.81	**32.13**	31.17
im-3	32.62	33.24	33.10	**33.57**	30.59
im-4	33.75	31.78	31.58	29.78	**33.85**
im-5	35.66	**37.51**	35.86	36.08	34.10
im-6	33.37	**36.21**	35.89	36.15	32.59
im-7	35.03	38.76	38.53	**40.24**	32.32
im-8	34.64	**38.33**	37.72	38.27	32.71
im-9	31.14	31.86	31.55	32.08	**32.71**
im-10	33.48	36.81	36.84	**38.22**	32.16
im-11	35.17	35.50	38.57	**39.65**	34.63
im-12	34.64	30.68	34.87	**36.74**	34.82
im-13	35.35	36.52	38.00	**39.10**	32.26
im-14	36.44	36.41	37.84	**38.57**	33.32

3.5 Summary

Both FT phase and the presented spatial domain constraints are closed and convex sets. They can be used as a part of well known blind deconvolution methods in an iterative manner in deblurring of microscopy images. This is possible due the microscopy image acquisition techniques involve symmetrical optical components and results in symmetrical blur like out of focus degradation. Furthermore slow moving cells makes it easy to assume that no motion blur is present. The extension of the Ayers-Dainty algorithm is made in a POCS manner. To this end, closed and convex sets are forced on the image in both spatial and Fourier domains. Apart from providing additional information, these projections also stabilize the end result of the algorithm. In our experiments, we observed that the introduction of FT phase and spatial domain constraints improve the performance of Ayers-Dainty method significantly in microscopy images.



(a) (b)

(c)

Figure 3.7: Immuno-fluorescense images of CD133 positive Huh7 liver cancer cells with differential focus: (a) x_f (top), (b) x_g (middle). The images x_f and x_g are combined to obtain (c) the deblurred image using Gaussian filtering based edge-enhancement together with phase and ESTV projections.

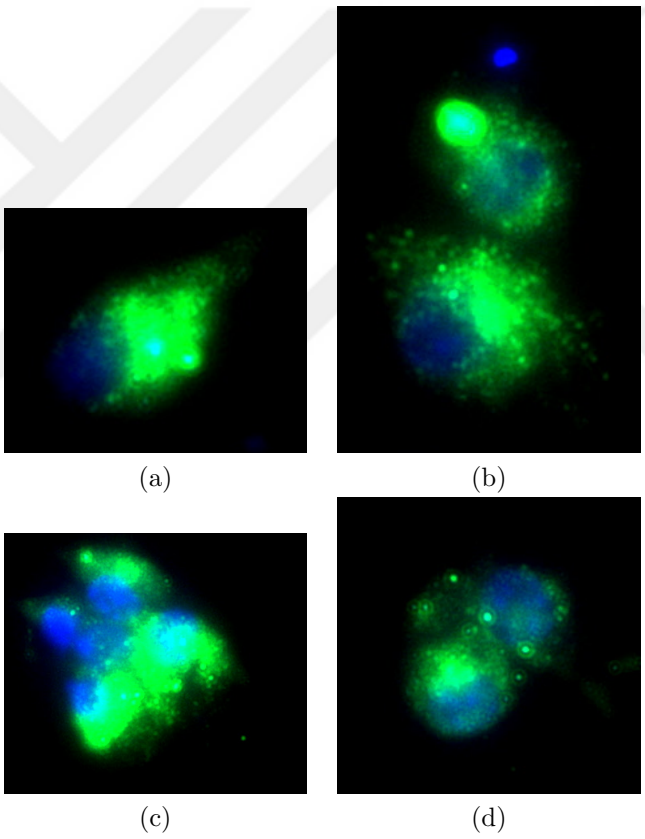


Figure 3.8: Sample fluorescent labeled mouse liver tissue images used in experiments (a) Im-1, (b) Im-2 (c) Im-3, and (d) Im-4 obtained from [2].

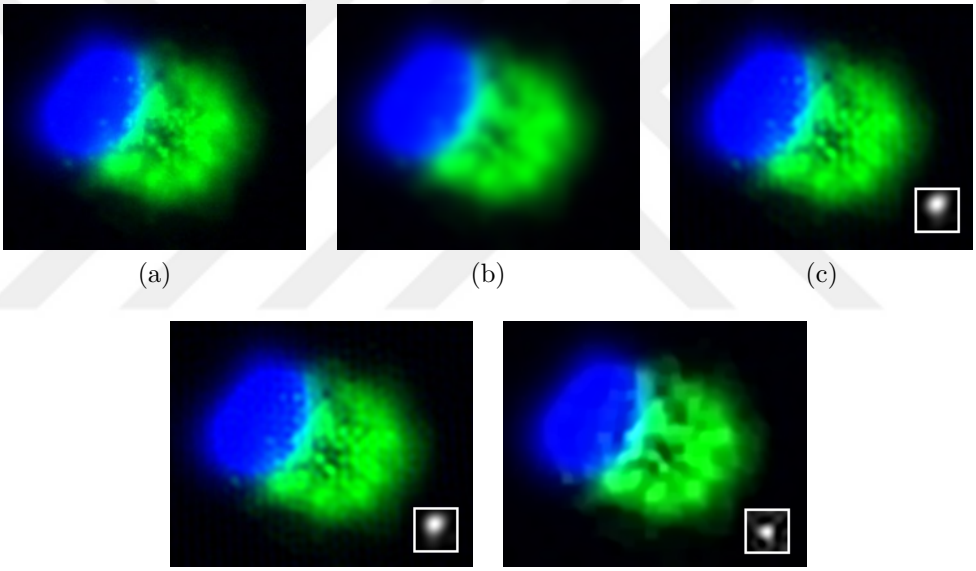


Figure 3.9: Sample deblurring results for "im-7": (a) Original image, (b) blurred image (Gaussian $\sigma = 5$); PSNR = 35.03 dB, (c) Image obtained by Ayers-Dainty with Phase and ESTV sets; PSNR = 40.24 dB, (d) Ayers-Dainty method; PSNR = 38.76 dB, (e) image obtained using [3]; PSNR = 32.32 dB. The blurring filter estimate for each case is shown in the bottom right corner.

Chapter 4

Fourier Transform Phase and Bounded Energy-based Deconvolution for Magnetic Particle Imaging

We present an POCS based iterative deconvolution algorithm applied onto Magnetic particle imaging (MPI). MPI is a new medical imaging research area [21, 22, 23], that has a wide spectrum of applications such as angiography [75, 76, 77], cancer research [78], stem cell tracking [79, 80], lung perfusion imaging [81], temperature mapping [82], and viscosity mapping [83]. The rest of the chapter is organized as follows: in Section 4.1, we present summary of the MPI research and its bottlenecks. In Section 4.2, we present the theoretical background and the utilized Fourier and spatial domain convex sets. We then give the simulation results in 4.3 and summarize the chapter in Section 4.4.

4.1 Previous Studies on Magnetic Particle Imaging

The basic principle of MPI is to monitor the magnetization response of super-paramagnetic iron oxide (SPIO) nanoparticles. The background tissue does not generate a response resulting in high contrast imaging.

It is possible to express MPI image as a result of convolution of the underlying structure (SPIO distribution) and a PSF [29, 30]. The spread parameters of the PSF depends on the size of the nanoparticle and and the gradient of the selection field. Higher selection field gradients can improve the sharpness of the resulting image, however this also yields a smaller field of view (FOV). Therefore a balance must be achieved between the FOV and image quality in MPI. Recent studies try to evaluate the safety and usability parameters of MPI for human use [24, 25, 26, 27, 28].

Another approach to human sized MPI problem is to process human body using small patches and then combining the results for larger imaging requirements [76]. One downsize of this procedure is the increase in total imaging time. A decrease in selection field strength may decrease the time at the expense of reduced resolution. In order to increase the graded image quality, Wiener deconvolution [31] and spatial-Fourier domain equalization [32] are previously utilized. However these techniques need the knowledge of the PSF which is not fully available in the MPI.

We utilize a blind deconvolution technique for recovering SPIO density from highly blurry MPI images. As discussed before, our main assumption is that the PSF is zero phase in meaningful area around origin in Fourier domain. As the assumption suggests, the Fourier transform phase of the original distribution and its reflection on the measurement (MPI image) are the same. We enforce this property as a projection in Fourier domain. Additionally, we further utilize spatial-domain constraint to limit the spatial support and regulate the spatial domain properties using projection onto ℓ_1 norm of the MPI images. We tested

the proposed technique against well-known Wiener and Lucy-Richardson deconvolution methods. Simulation results shows even though the PSF is available to the Wiener and Lucy-Richardson algorithms, the presented technique is superior in terms of recovery quality.

4.2 Methods

The presented algorithm employs POCS method that relies on Fourier transform phase in Fourier domain and, support and regularization convex sets in spatial domain. The PSF of the MPI is symmetrical in nature which makes an estimation of the Fourier phase of the original image from observation possible. The size of the spread and other spatial properties highly depends on the SPIO; it is not always possible to comment on the shape in real life MPI applications. In Figure 4.1 an example of the MPI PSFs is shown.

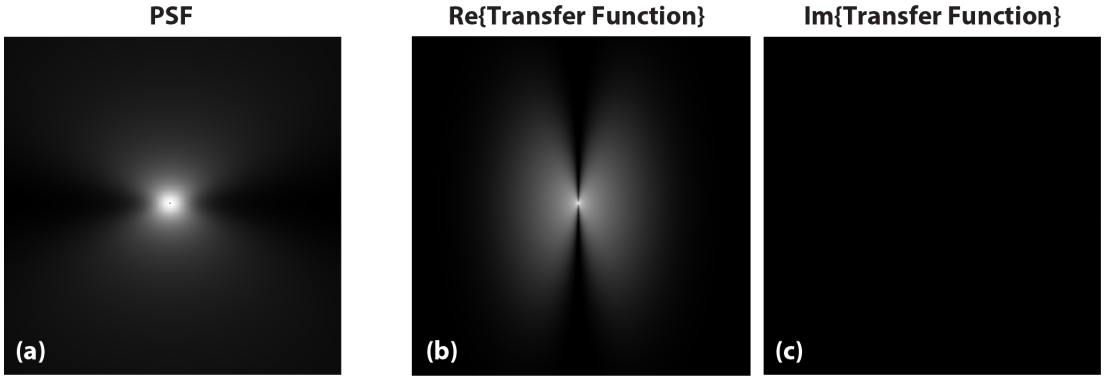


Figure 4.1: (a) Two-dimensional (2D) point spread function (PSF) of MPI. The corresponding transfer function is a zero-phase function. (b) The real part of the transfer function is positive-valued, and (c) the imaginary part is completely zero (here (b) and (c) are displayed with identical windowing).

The PSF has a symmetry around origin which results in a real valued Fourier transform coefficients. Figure 4.1 (b) and (c) demonstrates this mathematical property experimentally. We observe the PSF spread is dependent on the angle from the center, i.e., in this case, the spread is more on the horizontal direction compared to the vertical direction.

The zero phase property is, however not visible in this case. The Fourier transform coefficients may have negative values, however experiments show that this phenomena occurs around larger frequencies. The contribution of these frequencies to the image can be ignored and still a successful recovery can be achieved. These frequencies are also dependent on the spread which can be controlled by the size of the SPIO used.

Another property of MPI is the relaxation effect on the MPI observation. The physical causes and properties of this effect can be found in [30]. The spatial domain corresponding effect of this phenomena is a shift towards a side in the middle pixels of the PSF. The zero-phase property is disturbed by the effect. Furthermore, the shift seems to be relative to the magnitude of the PSF which depends on the spread, therefore indirectly depends on the SPIO size. Several experiments are made in order to investigate the robustness of the presented algorithm to the delay and blur effects of relaxation.

4.2.1 Fourier-Domain Phase Constraint

The properties of zero phase PSF and its usage in recovery of the original image Fourier transform phases is discussed in Chapter 2. We employ this property on MPI in the following equation:

$$g[n_1, n_2] = c_o[n_1, n_2] * h[n_1, n_2], \tag{4.1}$$

where $c_o[n_1, n_2] : \mathbb{Z}^2 \to \mathbb{R}_+$ is the 2D ideal MPI image, and $h[n_1, n_2] : \mathbb{Z}^2 \to \mathbb{R}_+$ is the PSF parameterized by the size of SPIO and the strength of the selection field. From the zero phase assumption we have,

$$\angle G(\omega_1, \omega_2) = \angle C_o(\omega_1, \omega_2) \tag{4.2}$$

Here, we assume that the following closed and convex set [70] based on phase

information is available in MPI:

$$S_\phi = \{c \mid \angle C(\omega_1, \omega_2) = \Phi(\omega_1, \omega_2)\} \tag{4.3}$$

where S_ϕ is the set of images that possess a given Fourier transform phase. This transform phase Φ is estimated from the phase of the observed blurred image $\angle\mathcal{F}\{g\}$. An orthogonal projection c_p of an MPI image c onto this set will enforce the desired phase property:

$$C_p(\omega_1, \omega_2) = |C(\omega_1, \omega_2)|.e^{j\Phi(\omega_1,\omega_2)} \tag{4.4}$$

where C_p is the DTFT of the projection image c_p and $|C(\omega_1, \omega_2)|$ is the magnitude of the DTFT of c. The projection operation simply replaces the phase of C with $\Phi(\omega_1, \omega_2)$.

The extraction of the phase $\Phi(\omega_1, \omega_2)$ from observed image includes spatial domain manipulations similar to that are done in Chapter 3. Here an estimate of non-cropped blurry image is obtained by replication of the boundaries [84]. For this purpose, we first stretch the boundary pixels of the observed blurry image in all directions as follows:

$$\hat{g}[n_1, n_2] = \begin{cases} g[n_1 - N_e, n_2 - N_e], & N_e \le n_1 \le N_e + N_1,\ N_e \le n_2 \le N_e + N_2 \\ g[n_1 - N_e, 0], & N_e \le n_1 \le N_e + N_1,\ n_2 < N_e \\ g[n_1 - N_e, N_2 - 1], & N_e \le n_1 \le N_e + N_1,\ n_2 > N_2 + N_e \\ g[0, n_2 - N_e], & N_e \le n_2 \le N_e + N_2,\ n_1 < N_e \\ g[N_1 - 1, n_2 - N_e], & N_e \le n_2 \le N_e + N_2,\ n_1 > N_1 + N_e \\ g[0, 0], & n_1 < N_e,\ n_2 < N_e \\ g[N_1 - 1, N_2 - 1], & n_1 > N_1 + N_e,\ n_2 > N_2 + N_e \\ g[0, N_2 - 1], & n_1 < N_e,\ n_2 > N_2 + N_e \\ g[N_1 - 1, 0], & n_2 < N_e,\ n_1 > N_1 + N_e \end{cases} \tag{4.5}$$

Here, $\hat{g}$ is the stretched image and N_e is the size of the extension. The size of the stretched image $\hat{g}$ then becomes $2N_e + N_1$ by $2N_e + N_2$.

Note that a pure stretching of the pixels at the image boundaries will not reflect the PSF-convolved output of the ideal image over an extended FOV. To

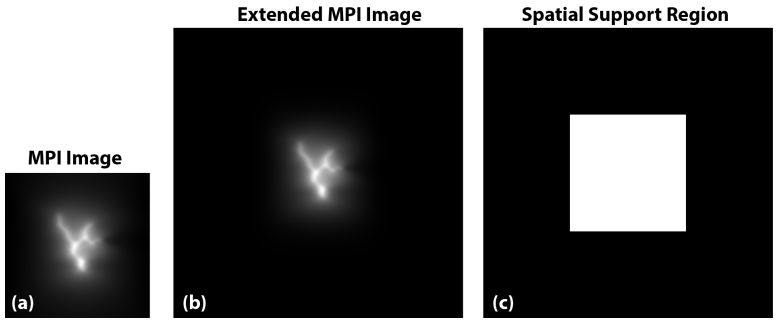


Figure 4.2: (a) The observed blurred MPI image, (b) its extended version, and (c) the support that marks the nonzero region used in spatial domain projections. Here, the spatial support is the same size as the imaging FOV, which is a very conservative estimate of the actual support of the MPI image.

closely mimic the effects of convolution via a natural PSF, the pixel intensities need to gradually fade to zero. To obtain such a gradual fading effect, we apply a gradient mask to the stretched image. This gradient mask is obtained by the convolution of the support s with a Gaussian low-pass filter.

$$s[n_1, n_2] = \begin{cases} 1, & N_e \leq n_1 \leq N_e + N_1, \;\; N_e \leq n_2 \leq N_e + N_2 \\ 0, & o.w. \end{cases} \tag{4.6}$$

This gradient mask is obtained by convolving the spatial support of the blurry image with a Gaussian filter of h_G with large variance (We chose σ as 10% of N_1 and N_2 in both directions). The final extended image $\tilde{g}$, is then obtained via multiplying the stretched image with the gradient mask.

$$\tilde{g} = \hat{g} \cdot (s * h_G). \tag{4.7}$$

These steps ensure that the extended image matches the observed image in central locations, while gradually fading to zero in the extended regions. The support obtained in Figure 4.2 is a conservative estimate of the actual support of the MPI image. In Figure 4.2, an example observed blurred image, its extended version, and the spatial support region are shown. For all steps of the proposed algorithm, the extended image support is utilized in iterations.

4.2.2 Spatial-Domain Support Constraint

The phase information in Eq. 4.4 is not sufficient to determine a solution to the inverse problem. One powerful solution is to constraint the spatial-domain support of the ideal image c_o, as proposed in magnitude retrieval algorithms studied in 1980s [39, 70, 85, 42]. Here we assume that the following closed and convex set based on support information is available:

$$S_s = \{c \mid c[n_1, n_2] = 0, \quad [n_1, n_2] \notin S\}, \tag{4.8}$$

where S is the spatial support of the ideal image c_o.

The projection c_s of an arbitrary image c onto the spatial-domain constraint set S_s is performed by simply retaining the portion of the image within the support region:

$$c_s[n_1, n_2] = \begin{cases} c[n_1, n_2], & if \quad [n_1, n_2] \in S \\ 0, & if \quad [n_1, n_2] \notin S \end{cases} \tag{4.9}$$

The support S is selected to be the original region of the blurry image before it is extended using the formulation expressed in Section 4.2.1. However it is possible to select this region in a way to exclude areas where the pixel values of the original image is known to be zero. For this study, we used a rectangular region as S, however, Section 4.2.3 presents another limitation on energy which may be utilized in the purpose of detection and filtering of zero pixels in the resulting image.

This step and the previous phase-constraint step are performed in an iterative manner, successively imposing the sets S_ϕ and S_S on the iterates [40, 70, 85, 42]. In practice, the precise support region S of the ideal MPI image may not be available. A reasonable choice for S would then be the imaging FOV (i.e., the region covered by the FFP trajectory), as done in this work. For that case, the spatial-domain constraint is equivalent to restricting the spatial support of the nanoparticle distribution to the FOV.

4.2.3 Spatial-Domain Regularization Constraint

Noise in MPI acquisitions can degrade the accuracy of the estimates for both the Fourier-domain phase and the spatial support, thereby compromising deconvolution performance. To improve performance, here we employ spatial the spatial domain regularization set discussed in Section 2.2.2 in our iterations.

This constraint is mainly used for denoising the results between iterations. However in MPI-like image reconstructions, projection onto ℓ_1 balls algorithm serves another purpose. The original image is known to have high contrast between the veins and the tissue. The black background tissue is represented by zero pixels are shadowed by the spreading particles in the observed image. However the true image is known to have these black pixels.

As the iterates slowly reduce the intensities of the background pixels, we use the presented ℓ_1 ball projection to zero out small values. The process does not need to be exact, therefore the projection in Section 2.2.2 can be effectively utilized.

4.2.4 The MPI Deconvolution Algorithm

Three closed and convex sets for Fourier-domain phase, spatial-domain support, and spatial regularization were defined in Sections 4.2.1-4.2.3. The proposed deconvolution algorithm employs iterative projections onto these sets, S_ϕ, S_s, and S_1^ϵ to simultaneously enforce the respective image properties. Let $c^{(k)}$ be the current, and $c^{(k+1)}$ be the next iterate for the deconvolved MPI image. The projections are implemented during the iterative deconvolution as follows:

$$c^{(k+1)} = P_1 P_s P_\phi(c^{(k)}), \tag{4.10}$$

where P_1 is the projection operator onto the ℓ_1 ball (Section 4.2.3), P_s is the projection operator onto the MPI spatial support set (Section 4.2.2) and P_ϕ is the projection operator onto the phase set (Section 4.2.1). Note that these projection operators do not rely on estimates of the imaging PSF at any stage. Since the

proposed algorithm does not utilize PSF information, it is a blind deconvolution method.

The POCS theorem [70] states that successive projections onto multiple sets will converge to a solution at the intersection of the sets, assuming that the intersection is non-empty. Thus iterates $c^{(k)}$ will converge to an image in $S_1 \cap S_s \cap S_\phi$ regardless of the initial image $c^{(0)}$. When the convex sets do not intersect, the iterates oscillate between three images satisfying either one of the sets S_1, S_s, and S_ϕ. At that point, the iterations and one of the above-mentioned solutions can be accepted as the solution to the inverse problem [86, 71, 87, 88]. In practice, iterations can be stopped when the difference between consecutive iterates become insignificant. In this work, it was observed that a total of 100 iterations were sufficient to obtain stable results.

In this work we compared the presented algorithm with the results of Wiener and Lucy-Richardson deconvolution methods. Note that neither of these algorithms is blind, but rather require information about the imaging PSF. Here, we utilized the exact PSF for both of these algorithms. The noise-to-signal power ratio parameter of Wiener deconvolution was set to 1.0. The iteration number parameter of Lucy-Richardson was set to 100. The ϵ parameter of the proposed ℓ_1 ball projection is, in each iteration set to be the 98% of the ℓ_1 norm of the iterate.

In the following parts, we give implementation details for the algorithm outlined in Equation 4.10. We first start by projecting the current image onto convex set S_ϕ defined by Equation 4.3. Because the PSF has zero phase characteristics, we assume that the ideal and observed MPI images carry identical phase information. However, this assumption is typically violated due to the finite FOV imaged, which causes the observed MPI image to be a truncated version of the full convolution of the ideal image and the PSF. This truncation forces a narrow rectangular support in spatial domain, which corresponds to a convolution in the Fourier domain that can disturb both the phase and magnitude of DTFT coefficients. Therefore, depending on the severity of the truncation, the phase information regarding the ideal image is only approximate.

4.2.5 Simulated MPI Acquisitions

We used a multi-dimensional x-space MPI simulation toolbox that we custom developed in MATLAB. This toolbox takes in parameters of an MPI scanner, together with nanoparticle size and relaxation time constant, and computes the MPI signal for a rectilinear trajectory using the multi-dimensional x-space formalism [30]. Here, all simulations utilized a selection field of (-6,3,3) $T/m/\mu_0$ in the x-,y-, and z-directions, respectively. Note that an MPI FFP scanner with comparable selection field characteristics was previously utilized in [76]. The nanoparticle diameter was assumed to be 25 nm, a reasonable value given the recent developments on tailored MPI nanoparticle synthesis [89]. The drive field in z-direction was at 25 kHz with 10 mT amplitude, which roughly covers a partial FOV size of 6.6 mm. An overall FOV of 4 cm by 4 cm was utilized in x- and z-directions, with an 80% overlap between partial FOVs along the z-direction to allow the recovery of the DC component that is lost due to filtering out of the fundamental harmonic [76]. The x-direction was rastered linearly. A single channel receive coil along the z-direction was utilized. The MPI signal was sampled with a sampling frequency of 25 MHz. At the chosen operating frequency and amplitude, a realistic relaxation time constant of $\tau = 0.5\mu s$ was incorporated based on previous experimental results at 25 kHz [90]. The relaxation effects were incorporated using an exponential kernel that convolves the ideal MPI signal:

$$s(t) = s_{adiab}(t) * r(t), \tag{4.11}$$

where

$$r(t) = \frac{1}{\tau} e^{-t/\tau} u(t). \tag{4.12}$$

Here, $s(t)$ is the signal with relaxation delays, $s_{adiab}(t)$ is the adiabatic MPI signal without relaxation delays and $u(t)$ is the Heaviside step function. This simple but powerful model was previously shown to provide a very good match to x-space MPI data across a wide range of drive field frequencies and amplitudes [90, 91].

We generated three sets of data for this part:

1. Blurred MPI Image: This image is simply the convolution of the nanoparticle distribution with the 3-dimensional MPI PSF [30].

2. Filtered MPI Images: These images take into account the fact that the fundamental harmonic is filtered out for the received MPI signal, typically using a notch filter centered around the drive field frequency. Each partial FOV is then reconstructed by first dividing the filtered MPI signal by the scanning speed and gridding the resulting image to the instantaneous position of the FFP [29]. A subsequent DC recovery algorithm was implemented using the smoothness of the overall MPI image [76]. We will refer to the resulting images as "filtered MPI images". Accordingly, filtered images at 9 different SNR levels were generated, by adding additive white Gaussian noise to the simulated MPI signal before the image reconstruction step.

3. Filtered MPI Images with Relaxation: When creating these images, the MPI signal was convolved with a relaxation kernel as given in Equation 4.11. Again, additive white Gaussian noise was added to this signal at 9 different SNR levels, followed by direct feed-through filtering. The images were reconstructed using the same procedure as described above.

The phantoms (i.e., ideal images) were sampled on a 4001×4001-pixel grid over an imaging FOV of $4cm \times 4cm$. The imaging PSFs were sampled on a 8001×8001-pixel grid, extending over a broad area when compared to the object itself. The full convolution output of the phantom and the imaging PSF was truncated to the original 4001×4001-pixel grid of the phantom to generate the blurred MPI images.

For the noisy image sets, a parameter called "signal SNR" was defined to quantify the degree of noise added. Accordingly, signal SNR was defined as the ratio of the peak signal that resulted during the scanning of the entire FOV, divided by the standard deviation of the added white Gaussian noise. We tested 8 different signal SNR levels between 5 dB and 40 dB, with steps of 5 dB. In addition, a zero-noise case (i.e., infinite signal SNR) was also tested. The x-space algorithm reconstructed a 201×4001 image (where 201 was the number

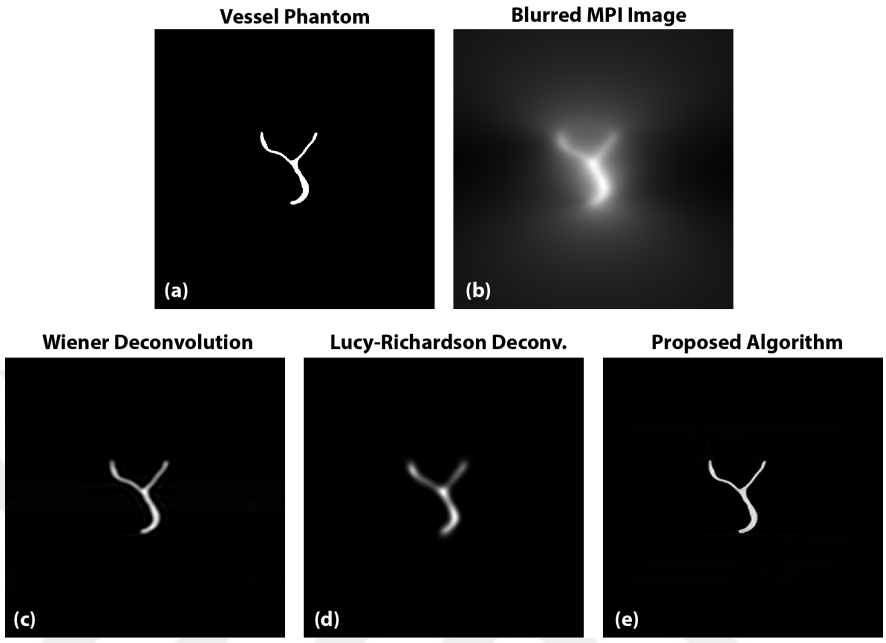


Figure 4.3: (a) The original vein phantom, (b) the observed MPI image assuming blurring due to an SPIO size of 25nm, but no acquisition noise (PSNR = 14.66dB with respect to the vein phantom). The results of (c) Wiener deconvolution (PSNR = 28.38dB), (d) Lucy-Richardson deconvolution (PSNR = 26.14dB), and (e) the proposed algorithm (PSNR = 32.26dB) after 100 iterations.

of lines scanned along the x-direction in the rectilinear trajectory), which was then fed to the proposed deconvolution algorithm. All images were interpolated to 4001×4001 for display purposes.

4.3 Simulation and Results

We demonstrate the proposed deconvolution algorithm on MPI images with significant blurring and relaxation effects. In our tests, we first processed a simple vein phantom to examine the progression of image recovery across iterations, for the case of an ideal x-space MPI image. The observed image was extended as described in Section 4.2.4 prior to POCS iterations, followed by blind deconvolution using the proposed algorithm. Wiener and Lucy-Richardson methods were performed for comparison.

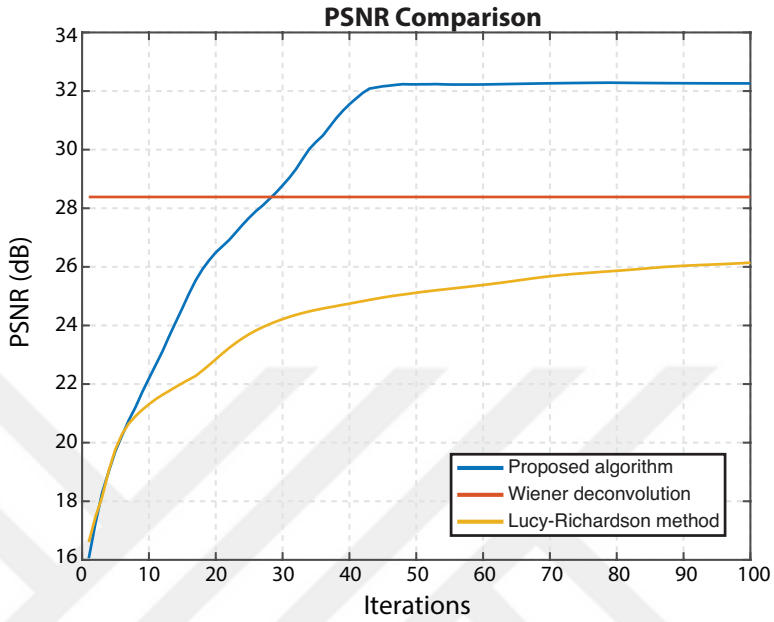


Figure 4.4: PSNR measured between the deconvolved image and the vein phantom (shown in Figure 4.3). Measurements are plotted as a function of the number of iterations for the Lucy-Richardson deconvolution and the proposed algorithm. Wiener deconvolution is displayed at a constant value, as it is a one-step algorithm. In this case, the proposed algorithm converges to a stable solution within 40 iterations, at significantly higher PSNR levels when compared to the other two methods.

The phantom image (i.e., the ideal image), the blurred x-space MPI image, and the deconvolution results are shown in Figure 4.3. The convergence speed and PSNR performance per iteration cycle of the proposed deconvolution algorithm are given in Figure 4.4. The Wiener method produces better edge emphasis than the Lucy-Richardson method, but it suffers from ringing artifacts due to resolution loss. Overall, although the Wiener and Lucy-Richardson methods are PSF-informed, they yield images with significant residual blurring and relatively low PSNR levels. This is despite the fact that a relatively large FOV when compared to the vessel size was utilized, which typically improves PSF-informed deconvolution results. In comparison, the proposed blind deconvolution method recovers a deblurred image with higher spatial resolution and PSNR, and one that visually matches the phantom image. The proposed method achieves 3.8dB higher PSNR than Wiener and 6.1dB higher PSNR than Lucy-Richardson deconvolution.

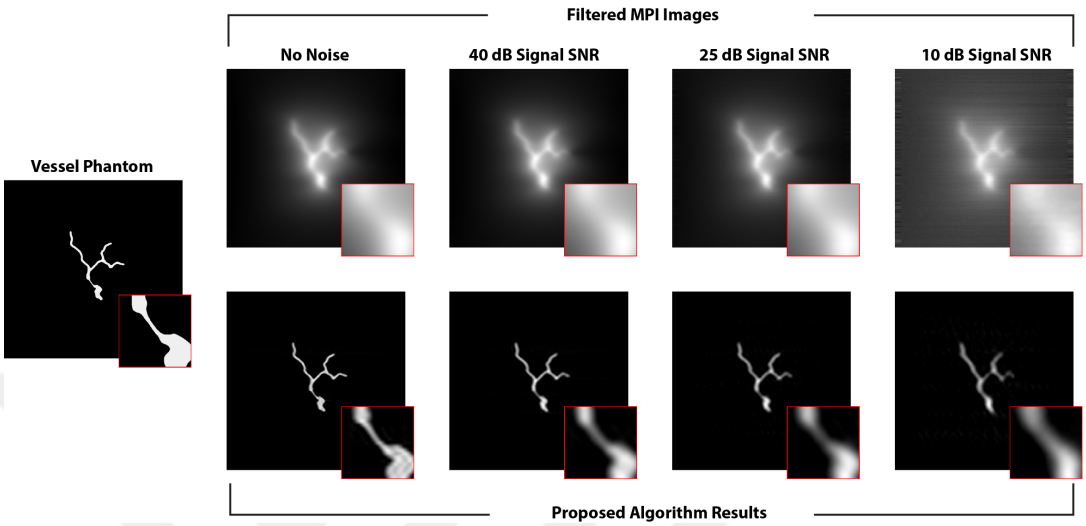


Figure 4.5: MPI images of a vessel phantom with stenosis in a vertically oriented vessel. The vessel phantom (left column). The reconstructed x-space MPI images at varying noise levels, with direct feedthrough filtering (top row). The deblurred images with the proposed blind deconvolution method (bottom row). From left to right: No noise, and 40dB, 25db and 10dB MPI signal SNR. A zoomed-in portion near the stenosis region is shown in small display windows at the corner of each image.

Spatial blurring in MPI images may pose a significant limitation to the accuracy of anatomical assessments. Deconvolution algorithms that recover the original spatial distribution of the nanoparticles from observed images can therefore be critical for many applications including MPI angiography. To examine the success of the proposed deconvolution in vascular assessment, we simulated two phantom images with stenoses in vertical and horizontal directions as shown in Figures 4.5 and 4.6, respectively. Filtered x-space MPI images at 9 different signal SNR levels were reconstructed to test the resilience of the proposed algorithm against noise. For the stenosis in the horizontal direction, nanoparticle relaxation effects were also incorporated.

The two original phantoms, the reconstructed x-space MPI images and the deconvolution results are shown in Figures 4.5 and 4.6. The proposed method produces deblurred images that accurately depict the vertical stenosis for signal SNR levels above 10 dB. In the x-space MPI images, especially horizontally-aligned blood vessels are blurred to a wide extent, and the depiction of these

vessels are clearly improved in the deconvolved results. Yet, the horizontal stenosis in Figure 4.6 can only be depicted for SNR levels above 25 dB. This difference is caused by the anisotropic shape of the MPI PSF; the PSF has much larger spread in vertical direction that severely fades the horizontal stenosis.

PSNR measurements of observed and deblurred images over a broad range of SNR levels are plotted in Figure 4.7. For the phantom with vertical stenosis, PSNR values are 29.39dB, 27.11dB, 25.64db, and 24.15dB, for no noise, 40dB, 25 dB, 10 dB signal SNR, respectively. For the phantom with horizontal stenosis (with relaxation), PSNR values are 28.41dB, 26.57dB, 25.44dB, and 24.01dB, for no noise, 40dB, 25 dB, 10 dB signal SNR, respectively. On average across SNR levels, the proposed method achieves 5.14dB higher PSNR than Wiener and 2.77dB higher PSNR than Lucy-Richardson deconvolution, without utilizing the imaging PSF.

4.4 Summary

We showed that the imaging PSF in MPI is a zero-phase filter in Fourier domain. We then proposed a new deconvolution technique that leverages this critical phase property. Our technique is based on iterative projections onto multiple convex sets, which reflect various constraints in Fourier and image domains. These constraints enforce consistency of Fourier-domain phase between observed and deconvolved images, and enforce an estimated spatial-domain support and low ℓ_1 norm for the deconvolved image.

The proposed algorithm offers numerous benefits over conventional deconvolution methods such as Wiener or Lucy-Richardson. First, unlike conventional methods, the proposed algorithm does not require any prior knowledge of the imaging PSF. It thereby performs blind deconvolution of MPI images. Second, it employs the computationally efficient FFT algorithm to transform between image and Fourier domains, and a fast approximate projection onto the ℓ_1 ball to

eliminate the complex sorting of pixel intensities. Thus it shows relatively improved convergence properties and computational efficiency. Lastly, the spatial regularization based on ℓ_1 norm in the image domain ensures enhanced reliability against high levels of noise in MPI images.

A number of technical advances can help further improve the deconvolution performance. The iterative POCS algorithm is initiated with the observed image. POCS theorem states that it is possible to start from any image and find a possible solution. Note, however, that if projected convex sets intersect at multiple points, the algorithm may converge onto distinct solutions depending on initialization. Here, we observed that initialization with the observed blurred image yields more desirable and consistent solutions than random initialization. It may further improve convergence if the algorithm was instead initiated with the Wiener deconvolution results estimated via an approximate PSF.

It would also be possible to improve performance if the exact PSF was available to the proposed algorithm. In gradually fading the support during Fourier phase extraction, we used a generic Gaussian PSF. The replacement of this filter with the known PSF may help improve precision of the estimated phase information, therefore improve the results. Since the algorithm would not be blind in that case, this approach was not investigated in this Chapter.

The proposed algorithm employed ℓ_1 regularization in the image domain for alleviating noise that corrupts MPI acquisitions. While ℓ_1 regularization of pixel intensities was observed to perform well here, other types of regularization terms could be incorporated to further improve noise resilience. For example, total-variation terms that assume a block-wise tissue structure can be powerful in noise suppression. Alternatively, ℓ_1-norm in a transform domain (e.g., wavelet domain) could be used to better enforce sparsity of MPI data. These terms can simply be included in the POCS algorithm as additional projections.

Here, we demonstrated a blind deconvolution algorithm for MPI based on comprehensive simulations incorporating noise, relaxation effects, and complex tissue structure (e.g., stenoses). Our results strongly indicate that the proposed

algorithm can enable accurate mapping of particle distribution in MPI. Numerous MPI applications from angiography to stem cell tracking can then benefit from the enhanced spatial acuity of deblurred MPI images. Further studies should be conducted to validate the current results and assess the reliability of the technique for in vivo imaging.

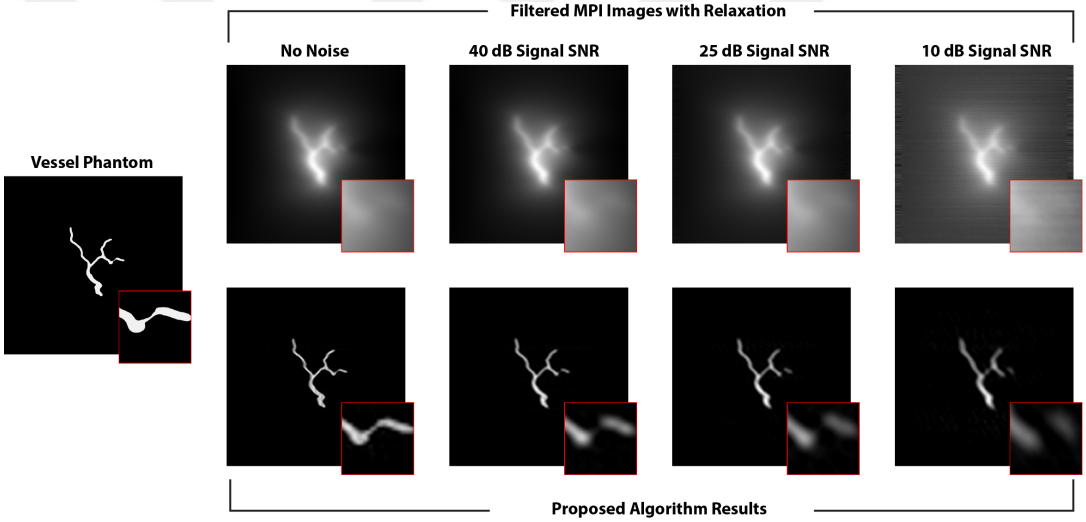


Figure 4.6: MPI images of a vessel phantom with stenosis in a horizontally oriented vessel. The vessel phantom (left column). The reconstructed x-space MPI images at varying noise levels, with direct feedthrough filtering and nanoparticle relaxation effects (top row). The deblurred images with the proposed blind deconvolution method (bottom row). From left to right: No noise, and 40dB, 25db and 10dB MPI signal SNR. A zoomed-in portion near the stenosis region is shown in small display windows at the corner of each image.

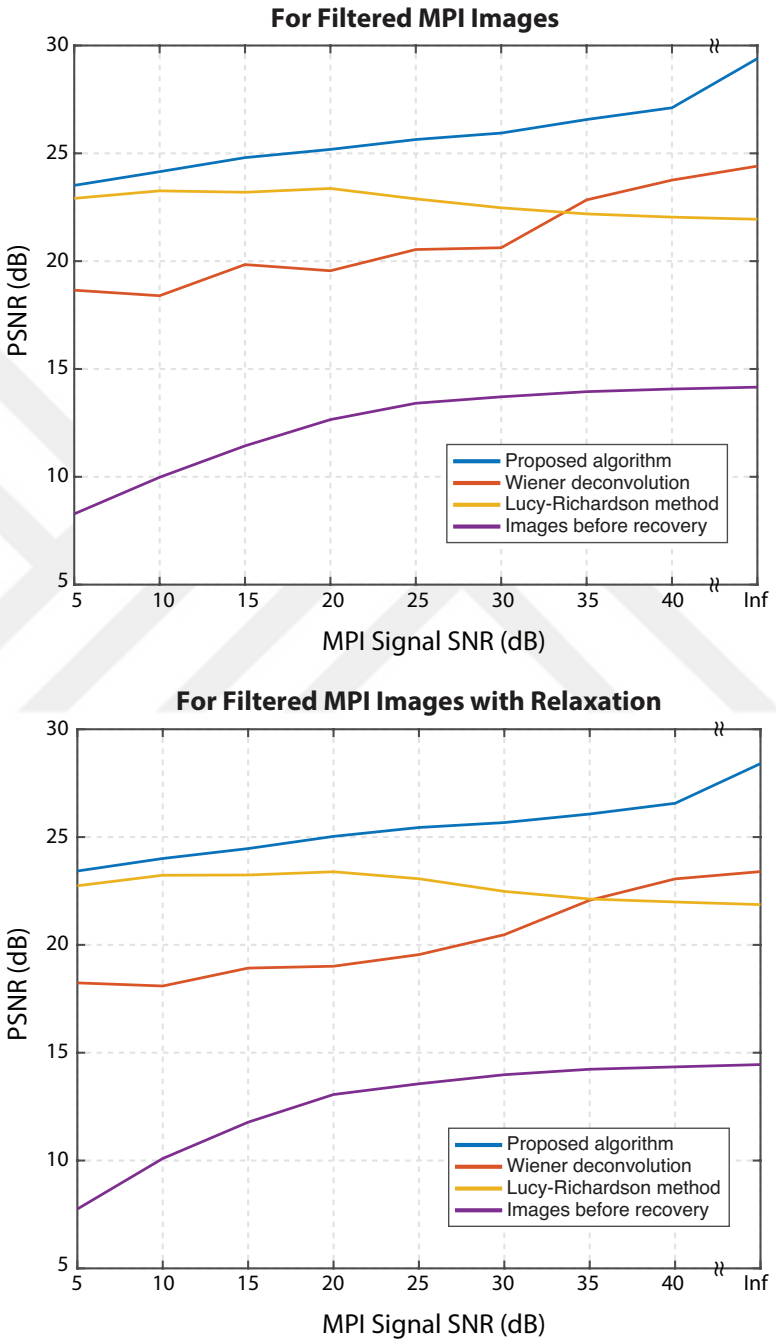


Figure 4.7: PSNR measurements were performed between the deconvolved images and phantoms, and between the x-space reconstructed images before recovery and phantoms. Deconvolution was performed separately via the Wiener, Lucy-Richardson methods, and the proposed algorithm. (a) Measurements as a function of the MPI signal SNR level for direct feedthrough filtered case. (b) Measurements as a function of the MPI signal SNR level for direct feedthrough filtered case that also incorporates nanoparticle relaxation effects.

Chapter 5

Phase-based Iterative Deconvolution

We present a Fourier phase and bounded energy based deconvolution method in order to recover images from filtered versions with known PSF. The proposed iterative deconvolution method does not require zero-phase or symmetry property of the PSF. Therefore, the method can be utilized for more general applications.

The rest of the chapter is organized as follows: In Section 5.1, we review the well-known Wiener deconvolution method that is used as basis for the proposed algorithm. We then present Fourier and spatial domain constraints used in proposed algorithm in Section 5.2. We then present the results of the experiments and summarize the chapter.

5.1 Review of Wiener Deconvolution

Wiener deconvolution is a well-known method that is based on the Fourier domain relation of the observed image, original image, the blurring filter and noise components.

The method is widely used in many image deblurring problems including applications discussed in this thesis such as microscopy image reconstruction [33, 34] and recovery of MPI images [35]. The algorithm is defined as follows:

Let $x[n_1, n_2]$ be an image, $h[n_1, n_2]$ be a filter. Then the observed image in many imaging applications is:

$$y[n_1, n_2] = (x * h)[n_1, n_2] + w[n_1, n_2], \tag{5.1}$$

where $w[n_1, n_2]$ is a zero mean Gaussian noise. The Wiener deconvolution aims to find a filter $g[n_1, n_2]$ that is the inverse of $h[n_1, n_2]$, such that:

$$\hat{x}[n_1, n_2] = (y * g)[n_1, n_2], \tag{5.2}$$

where $\hat{x}[n_1, n_2]$ is the approximation of original image $x[n_1, n_2]$. The Fourier transform of the deconvolution filter $g[n_1, n_2]$ is defined by:

$$G(\omega_1, \omega_2) = \frac{H^*(\omega_1, \omega_2) S_Y(\omega_1, \omega_2)}{|H(\omega_1, \omega_2)|^2 S_Y(\omega_1, \omega_2) + S_W(\omega_1, \omega_2)}, \tag{5.3}$$

where superscript $(^*)$ is the complex conjugate operation. $H(\omega_1, \omega_2)$ and $G(\omega_1, \omega_2)$ are the DTFTs of $h[n_1, n_2]$ and $g[n_1, n_2]$, respectively, and $S_W(\omega_1, \omega_2)$ and $S_Y(\omega_1, \omega_2)$ are the power spectral densities of $w[n_1, n_2]$ and $x[n_1, n_2]$, respectively.

The deconvolution filter $g[n_1, n_2]$ can be obtained through inverse Fourier transform of $G(\omega_1, \omega_2)$. The Wiener deconvolution obtains the estimate image $\tilde{x}[n_1, n_2]$ of the original image $x[n_1, n_2]$ as follows:

$$\tilde{x}[n_1, n_2] = (g * y)[n_1, n_2]. \tag{5.4}$$

When re-written, Equation 5.3 becomes:

$$G(\omega_1, \omega_2) = \frac{1}{H(\omega_1, \omega_2)} \left[\frac{|H(\omega_1, \omega_2)|^2}{|H(\omega_1, \omega_2)|^2 + \frac{S_W(\omega_1, \omega_2)}{S_Y(\omega_1, \omega_2)}} \right] \tag{5.5}$$

From Equation 5.5, we observe that if there is no noise component, the Fourier transform of deconvolution filter simply becomes $1/H(\omega_1, \omega_2)$. A simple division operation given in Equation 5.5 is expected because the corresponding operation of spatial domain convolution is multiplication in Fourier domain. In the presence of noise, the power spectral density of the noise is not always fully known. Therefore in many Wiener deconvolution applications, the power spectral density ratio $S_W(\omega_1, \omega_2)/S_Y(\omega_1, \omega_2)$ is selected as a constant. Equation 5.5 becomes:

$$G(\omega_1, \omega_2) = \frac{H^*(\omega_1, \omega_2)}{|H(\omega_1, \omega_2)|^2 + \frac{S_W(\omega_1, \omega_2)}{S_Y(\omega_1, \omega_2)}} \tag{5.6}$$

and

$$G(\omega_1, \omega_2) = \frac{1}{H(\omega_1, \omega_2) + K} \tag{5.7}$$

where K is the empirically selected constant.

5.2 TV and Fourier phase based deconvolution method for general filter types

We present an algorithm that aims to deconvolve blurry observation images with known blurring filters.

5.2.1 Fourier phase constraint

We utilized the Fourier phase and magnitude knowledge of the PSF as a Fourier domain information. Unlike previously described algorithms, this algorithm does not require the PSF to have a zero phase or symmetrical. The relationship in Equation 2.2 yields the following phase property:

$$\angle Y(\omega_1, \omega_2) = \angle X(\omega_1, \omega_2) + \angle H(\omega_1, \omega_2), \tag{5.8}$$

in the absence of noise. When there is noise we have:

$$\tilde{y}[n_1, n_2] = y[n_1, n_2] + w[n_1, n_2], \tag{5.9}$$

and the corresponding Fourier domain relation is given by:

$$\tilde{Y}(\omega_1, \omega_2) = X(\omega_1, \omega_2)H(\omega_1, \omega_2) + W(\omega_1, \omega_2) \tag{5.10}$$

where $W(\omega_1, \omega_2)$ is the DTFT of the noise component $w[n_1, n_2]$ and $\tilde{Y}(\omega_1, \omega_2)$ is the DTFT of the noisy observation $\tilde{y}[n_1, n_2]$. The phase relation given in Equation 5.8 is disturbed due the additive noise. The noise component of resulting $\tilde{Y}(\omega_1, \omega_2)$ is negligible if $Y(\omega_1, \omega_2)$ is considerably larger than $W(\omega_1, \omega_2)$ for given ω_1 and ω_2. For such frequencies, Equation 5.8 can be considered to hold. For such frequencies we can write the following relation for the magnitude of the original image:

$$|\hat{X}(\omega_1, \omega_2)| = \frac{|\tilde{Y}(\omega_1, \omega_2)|}{|H(\omega_1, \omega_2)|} \tag{5.11}$$

and in Fourier domain, we estimate the phase of the original image as follows:

$$\angle\hat{X}(\omega_1, \omega_2) = \angle\tilde{Y}(\omega_1, \omega_2) - \angle H(\omega_1, \omega_2) \tag{5.12}$$

The Equation 5.11 can be used only in frequencies where $H(\omega_1, \omega_2)$ is not zero. Therefore we can confidently recover the Fourier transform components only if the magnitude value of $H(\omega_1, \omega_2)$ is sufficiently large. However many blurring filters are low-pass in nature since the filters have a tendency to eliminate many of the high frequency components in frequency domain. Furthermore, high noise can manipulate the phase and magnitude greatly in small valued Fourier coefficients. As a result, estimation of a limited amount of frequency components is not enough to recover the original image from magnitude information. On the other hand phase information is more reliable than magnitude [39].

5.2.1.1 Implementation

In practice, natural images have larger components in lower frequencies. Furthermore, many image acquisition techniques also have low-pass nature. In general, using Equations 5.11 and 5.12, we can recover most of the low frequency components. However for small $|H(\omega_1, \omega_2)|$, the Fourier magnitude and phase obtained from Equations 5.11 and 5.12 may not be reliable. Therefore in the iterative algorithm, phase and magnitudes of the Fourier domain iterate are updated as follows:

$$\angle \hat{X}_i(\omega_1, \omega_2) = \begin{cases} \angle Y(\omega_1, \omega_2) - \angle H(\omega_1, \omega_2), & if\ |Y(\omega_1, \omega_2)| > 3\sigma\ and \\ & |H(\omega_1, \omega_2)| > \alpha \\ \angle \hat{X}_{i-1}(\omega_1, \omega_2), & otherwise \end{cases} \tag{5.13}$$

and

$$|\hat{X}_i(\omega_1, \omega_2)| = \begin{cases} \frac{1}{2}\left|\left(\frac{Y(\omega_1,\omega_2)}{H(\omega_1,\omega_2)}\right)\right| + \frac{1}{2}|\hat{X}_{i-1}(\omega_1, \omega_2)|, & if\ |Y(\omega_1, \omega_2)| > 3\sigma\ and \\ & |H(\omega_1, \omega_2)| > \alpha. \\ |\hat{X}_{i-1}(\omega_1, \omega_2)|, & otherwise \end{cases} \tag{5.14}$$

where α is a predetermined value that is sufficiently large for division, and σ is the standard deviation of noise, if known. In Equation 5.14 we have a relaxed projection operation.

The estimate image $\hat{x}[n_1, n_2]$ found by inverse Fourier transform of $\hat{X}(\omega_1, \omega_2)$ may not be sufficiently regularized for a successful image reconstruction. In the next section we incorporate the Total Variation (TV) regularization to the above iterative process.

5.2.2 TV-based Regularization

The TV based regularization method is applied on the iterates $\hat{x}_i[n_1, n_2]$ in the spatial domain. Utilized TV regularization method is similar to the one explained

in Chapter 3. We start by dividing the image $\hat{x}_i[n_1, n_2]$ into its high and low frequency components using a simple low pass filter $h_{lp}[n] = [0.25, 0.5, 0.25]$. In 2D, the filter is calculated as follows:

$$h_{lp}[n_1, n_2] = h_{lp}[n] * h_{lp}^T[n]. \tag{5.15}$$

Resulting 2D 3×3 filter is used to obtain the low pass component of the image:

$$\hat{x}_{ilp}[n_1, n_2] = (h_{lp} * \hat{x}_i)[n_1, n_2]. \tag{5.16}$$

Then the high frequency components are found by

$$\hat{x}_{ihp}[n_1, n_2] = \hat{x}_i[n_1, n_2] - \hat{x}_{ilp}[n_1, n_2]. \tag{5.17}$$

We apply TV reduction on $\hat{x}_{hp}[n_1, n_2]$ in order to requlate the spatial domain image. For this, we calculate the ℓ_1 norm of the image $\hat{x}_{hp}[n_1, n_2]$. We define a projection onto ϵ ball set S_ϵ which is defined as follows:

$$S_\epsilon = \left\{ x[n_1, n_2] | \sum_{n_1, n_2} |x[n_1, n_2]| \leq \epsilon \right\}. \tag{5.18}$$

Since the images are positive S_ϵ becomes:

$$S_\epsilon = \left\{ x[n_1, n_2] | \sum_{n_1, n_2} x[n_1, n_2] \leq \epsilon \right\}. \tag{5.19}$$

We select the ϵ to be a portion of the ℓ_1 norm of the image $\hat{x}[n_1, n_2]$. Instead of calculating a full projection, we repeat the procedure explained in Section 2.2.2.

The applied regularization enables us to recover an estimate of the original image $\hat{x}$ in an iterative manner. In each iteration we correct phases with large enough magnitude on Fourier domain. In spatial domain, we first apply a support generated by the extension of image for Fourier phase extraction as described in

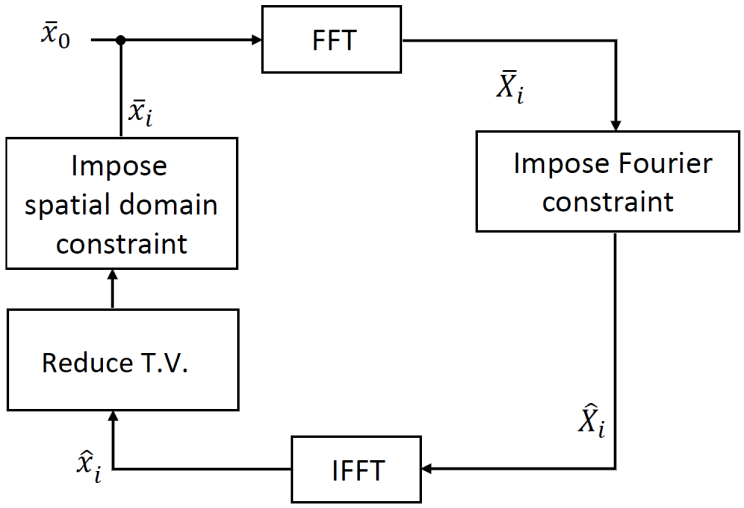


Figure 5.1: Flow-chart of the proposed Fourier phase and TV reduction based algorithm.

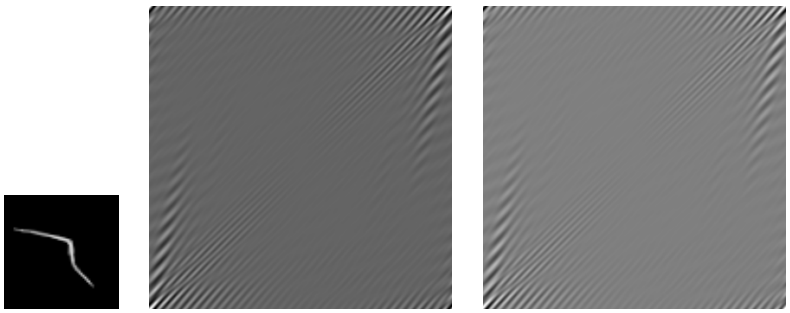
Section 4.2.1 in detail. We then apply the TV regularization algorithm in spatial domain in each iteration. The flow chart of the described iterative algorithm is as given in Figure 5.1.

It should be pointed out that the low-pass filter $h_{lp}[n_1, n_2]$ can be implemented without performing any multiplications because the coefficients of the filter are powers of 2.

Projection onto S_ϵ is described in Section 2.2.2 and it requires only one division operation and N subtractions.

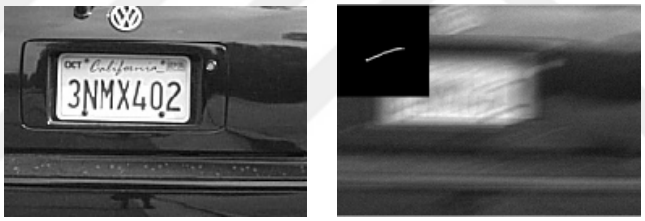
5.3 Experimental Results

In order to test the proposed algorithm, we used four motion blur type filters. The filters are selected to be non-symmetrical with irregular patterns. This yields complex Fourier transform coefficients and non-zero phase values in many frequencies. One of the filters used in our experiments are shown with its Fourier response in Figure 5.2.



(a) (b) (c)

Figure 5.2: (a) A 60 × 60 non-symmetrical filter used in this study. (b) The real part and (c) imaginary part of 256×256 point DFT of this filter shows that the Fourier domain phases are non-zero. The dynamic range of (b) and (c) are normalized to display the DFT.



(a) (b)

Figure 5.3: (a) Cropped version of the image "image_0111.jpg" from the database in [4] and (b) the blurred version of this image with noise ($\sigma = 1.5e - 4$). The blurring filter is shown on top left corner of (b). The range of the image pixels intensities is [0, 1].

These curved line filters are used in simulating the blur caused by motion. In this work, we addressed a plate number recognition problem in order to evaluate the performance of the proposed algorithm. We first filtered various plate images with large motion blur filters and then applied noise. We used a rear car image dataset available in [4]. We selected the last 15 images from this dataset eliminating the ones with unreadable plate numbers. An example image and its filtered version is given in Figure 5.3.

We compared the results of the presented method with well-known Wiener deconvolution. The similarities in implementations and usage of both algorithms make them comparable. Both algorithms rely on division of observed image with the filter in Fourier domain. The major difference arise from selective usage of

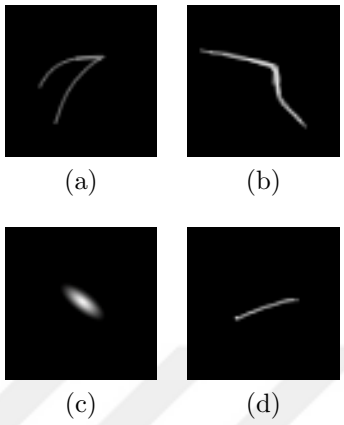


Figure 5.4: Various filters used in deconvolution studies: (a) filter1, (b) filter2, (c) filter3 and (d) filter4 used in the tests. The size of the images are 60×60.

Fourier transform phase and magnitudes and spatial domain TV reduction based regularization.

Motion blur in images captured from surveillance cameras are caused by motion of the vehicle being captured. Therefore a PSF that spreads on a curved line in the direction of motion is expected. However a more general problem can be defined as camera shake due to the wind shaking the masts the cameras are attached to. In our tests, we used four different non symmetrical blurring filters to simulate more general cases of blur as shown in Figure 5.4.

In the TV reduction algorithm, we limited the power of high frequency components to 80% of the total power of current iterate. We also set the α to be equivalent to three times the noise sigma. We limited the maximum number of iterations to 10. However if the difference between the consecutive iterates are less than a predetermined β we stopped the iterations. The results of the tests are given in Tables 5.1 - 5.4. In these tests we utilize PSNR as the performance measure. We tested our algorithm against various noise levels.

The PSNR comparison of deconvolved images yield that even the camera shake patterns are highly irregular, the proposed algorithm may still result high quality recovery. When we investigate the results we see the lowest quality of recovery results for the proposed method are the images that are filtered with “filter3”.

Table 5.1: PSNR Results of the deconvolution of proposed method and Wiener deconvolution methods on blurred images with "filter1".

	Wiener Filter				Proposed Method			
Noise σ (PSNR)	5×10^{-5}	7.5×10^{-5}	10^{-4}	1.5×10^{-4}	5×10^{-5}	7.5×10^{-5}	10^{-4}	1.5×10^{-4}
image_0112.jpg	21.73	21.57	21.40	21.13	**22.77**	**22.65**	**22.45**	**22.03**
image_0113.jpg	15.19	15.29	15.39	15.52	**18.78**	**18.48**	**18.37**	**18.13**
image_0114.jpg	24.16	24.45	24.53	24.59	**26.18**	**26.21**	**25.92**	**25.51**
image_0117.jpg	19.41	19.46	19.40	19.43	**20.43**	**20.21**	**19.91**	**19.76**
image_0118.jpg	15.85	16.12	16.32	16.57	**20.33**	**20.24**	**20.24**	**20.21**
image_0119.jpg	17.42	17.73	17.87	18.06	**18.54**	**18.42**	**18.34**	**18.24**
image_0121.jpg	17.30	17.77	18.12	18.54	**20.84**	**20.40**	**20.23**	**20.60**
image_0122.jpg	16.63	16.92	17.10	17.29	**19.33**	**19.26**	**19.22**	**19.22**
image_0123.jpg	17.04	17.29	17.36	17.48	**18.14**	**18.12**	**18.07**	**18.01**
image_0124.jpg	12.28	12.54	12.79	13.15	**18.36**	**18.19**	**17.98**	**17.82**
image_0125.jpg	15.31	15.76	16.03	16.45	**17.05**	**16.75**	**16.71**	**16.75**
image_0126.jpg	24.24	24.43	24.55	24.50	**27.43**	**26.88**	**26.63**	**25.97**
image_0108.jpg	**18.38**	**18.52**	**18.64**	**18.68**	18.02	17.57	17.42	17.18
image_0110.jpg	8.45	8.73	8.99	9.33	**18.71**	**18.35**	**18.30**	**18.21**
image_0111.jpg	14.16	14.43	14.58	14.87	**19.46**	**19.26**	**19.10**	**19.25**

Table 5.2: PSNR Results of the deconvolution of proposed method and Wiener deconvolution methods on blurred images with "filter2".

	Wiener Filter				Proposed Method			
Noise σ (PSNR)	5×10^{-5}	7.5×10^{-5}	10^{-4}	1.5×10^{-4}	5×10^{-5}	7.5×10^{-5}	10^{-4}	1.5×10^{-4}
image_0112.jpg	20.55	20.65	20.59	20.49	**22.35**	**22.19**	**21.91**	**21.49**
image_0113.jpg	14.27	14.71	15.00	15.34	**17.10**	**16.96**	**16.96**	**16.90**
image_0114.jpg	22.80	23.22	23.45	23.63	**24.58**	**24.67**	**24.50**	**24.34**
image_0117.jpg	18.18	18.55	**18.76**	**18.93**	**18.93**	**18.67**	18.76	18.88
image_0118.jpg	14.22	15.05	15.54	16.07	**19.53**	**19.58**	**19.76**	**19.80**
image_0119.jpg	16.17	16.67	16.94	17.17	**17.53**	**17.35**	**17.37**	**17.49**
image_0121.jpg	16.65	17.40	17.85	18.42	**18.64**	**18.83**	**19.33**	**20.29**
image_0122.jpg	14.69	15.12	15.35	15.52	**18.16**	**18.14**	**18.18**	**17.95**
image_0123.jpg	16.15	16.32	16.38	16.42	**17.25**	**17.38**	**17.41**	**17.33**
image_0124.jpg	7.76	8.83	9.58	10.61	**17.01**	**16.80**	**16.75**	**16.79**
image_0125.jpg	14.88	15.41	15.71	16.01	**15.17**	**15.42**	**15.76**	**16.56**
image_0126.jpg	23.28	23.69	23.89	24.05	**26.48**	**25.99**	**25.83**	**25.41**
image_0108.jpg	**16.73**	**17.03**	**17.25**	**17.41**	15.44	15.55	15.81	16.29
image_0110.jpg	4.81	5.94	6.71	7.71	**17.16**	**17.10**	**17.19**	**17.43**
image_0111.jpg	12.06	12.91	13.47	14.10	**18.20**	**18.41**	**18.61**	**18.94**

Table 5.3: PSNR Results of the deconvolution of proposed method and Wiener deconvolution methods on blurred images with "filter3".

	Wiener Filter				Proposed Method			
Noise σ (PSNR)	5×10^{-5}	7.5×10^{-5}	10^{-4}	1.5×10^{-4}	5×10^{-5}	7.5×10^{-5}	10^{-4}	1.5×10^{-4}
image_0112.jpg	**20.18**	**20.17**	**20.17**	**20.13**	19.25	19.88	19.88	19.89
image_0113.jpg	10.33	12.14	13.18	**14.42**	**11.17**	**13.02**	**14.12**	14.27
image_0114.jpg	**25.28**	**25.33**	**25.31**	**25.26**	25.01	25.10	25.12	25.10
image_0117.jpg	**17.88**	**18.42**	**18.69**	**18.91**	14.65	15.89	15.87	16.16
image_0118.jpg	**17.89**	**18.55**	**18.88**	19.20	16.45	17.23	18.32	**19.46**
image_0119.jpg	**17.08**	**17.13**	**17.12**	**17.07**	14.87	15.04	15.16	15.39
image_0121.jpg	**18.10**	**18.97**	**19.46**	**19.90**	16.50	17.11	17.50	18.64
image_0122.jpg	15.44	15.86	16.11	16.29	**15.83**	**15.98**	**16.22**	**16.75**
image_0123.jpg	**16.70**	**17.06**	17.23	17.40	15.47	16.36	**17.28**	**17.41**
image_0124.jpg	11.02	12.67	13.64	**14.75**	**11.64**	**13.75**	**14.08**	14.21
image_0125.jpg	**14.50**	**15.41**	**15.86**	**16.28**	11.69	13.97	14.63	15.15
image_0126.jpg	**25.71**	**25.74**	**25.71**	**25.59**	25.54	25.55	25.54	25.40
image_0108.jpg	**16.46**	**16.68**	**16.74**	**16.84**	10.91	13.51	14.11	14.63
image_0110.jpg	8.26	9.97	11.04	12.31	**14.32**	**14.59**	**14.83**	**15.20**
image_0111.jpg	13.79	14.97	15.61	**16.37**	**15.35**	**15.86**	**15.79**	16.33

Table 5.4: PSNR Results of the deconvolution of proposed method and Wiener deconvolution methods on blurred images with "filter4".

	Wiener Filter				Proposed Method			
Noise σ (PSNR)	5×10^{-5}	7.5×10^{-5}	10^{-4}	1.5×10^{-4}	5×10^{-5}	7.5×10^{-5}	10^{-4}	1.5×10^{-4}
image_0112.jpg	19.73	19.89	19.95	20.05	**22.77**	**22.52**	**22.21**	**21.84**
image_0113.jpg	9.77	10.13	10.44	10.92	**19.80**	**19.55**	**19.29**	**18.87**
image_0114.jpg	23.34	23.72	24.00	24.32	**26.51**	**25.93**	**25.80**	**25.61**
image_0117.jpg	17.61	17.79	17.93	18.24	**21.25**	**20.82**	**20.50**	**20.04**
image_0118.jpg	17.62	18.12	18.45	18.91	**21.48**	**21.22**	**21.02**	**20.68**
image_0119.jpg	17.31	17.67	17.87	18.15	**18.75**	**18.55**	**18.38**	**18.16**
image_0121.jpg	15.29	15.99	16.44	17.09	**21.94**	**21.03**	**20.60**	**20.11**
image_0122.jpg	14.18	14.71	15.14	15.71	**19.36**	**19.14**	**18.99**	**18.75**
image_0123.jpg	14.42	15.13	15.66	16.39	**20.09**	**19.93**	**19.76**	**19.58**
image_0124.jpg	8.92	9.42	9.83	10.42	**17.69**	**17.73**	**17.63**	**17.35**
image_0125.jpg	13.72	14.36	14.83	15.46	**18.38**	**17.89**	**17.42**	**16.96**
image_0126.jpg	25.17	25.45	25.56	25.54	**27.44**	**26.80**	**26.48**	**25.93**
image_0108.jpg	15.90	16.25	16.44	16.76	**18.63**	**17.95**	**17.56**	**16.83**
image_0110.jpg	9.14	9.68	10.12	10.73	**19.50**	**19.04**	**18.59**	**18.33**
image_0111.jpg	14.76	15.25	15.62	16.05	**20.13**	**19.79**	**19.48**	**19.18**

This filter is relatively large in spread in all directions where the others spread mostly in a single direction. Such cases may arise from the camera shake or the object motion captured with an out of focus imaging device. One of the reasons that the proposed system fails to recover successfully is that the usable frequency phase information is highly limited due that the large spread of PSF which means few non-zero elements around origin in Fourier domain. Many of the phases are excluded because of the process that aims to select reliable phases which is described in Equation 5.13.

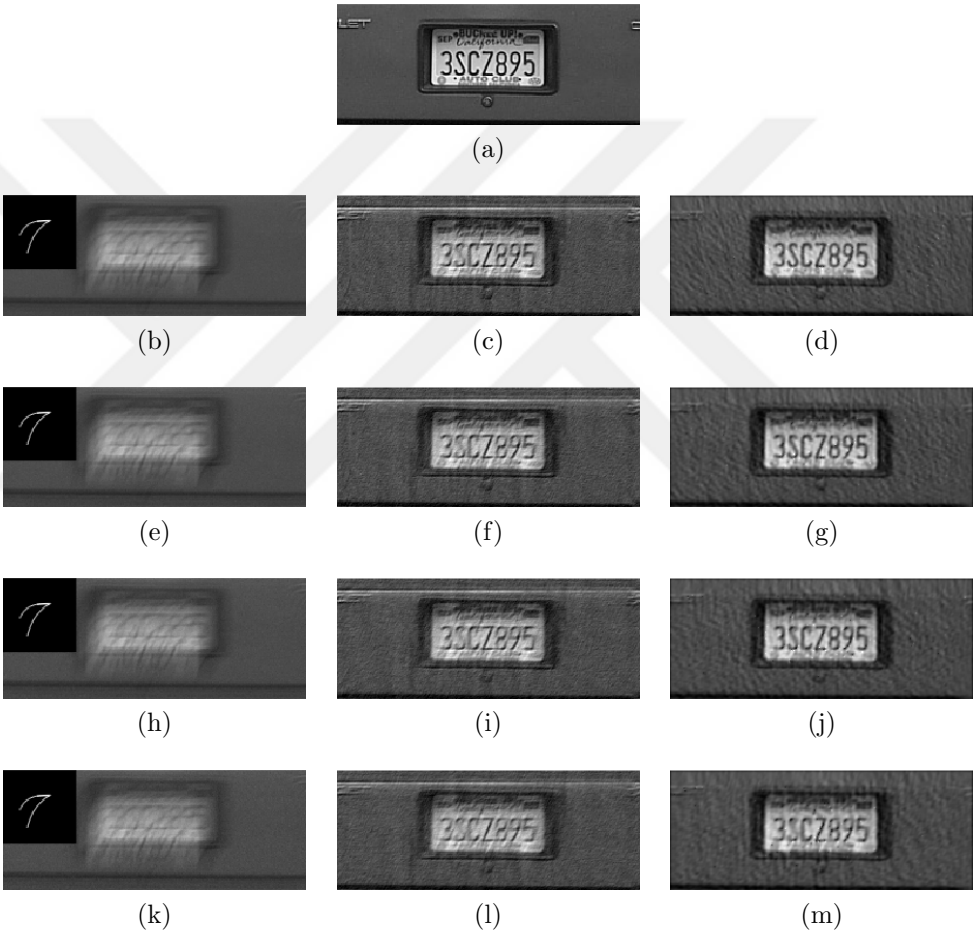
A visual comparison is also required for better understanding of the outcome quality. Figures 5.5 to 5.8 shows results of experiments for various filters and noise levels in different images.

As stated before, the number of iterations are limited to 10 in this study, furthermore we stopped iterations when the error between successive iterates are small. In Figure 5.9, we show that the iteration limit is sufficient for the images tested in this work. We observe that the PSNR is stable after the 5th iteration.

5.4 Summary

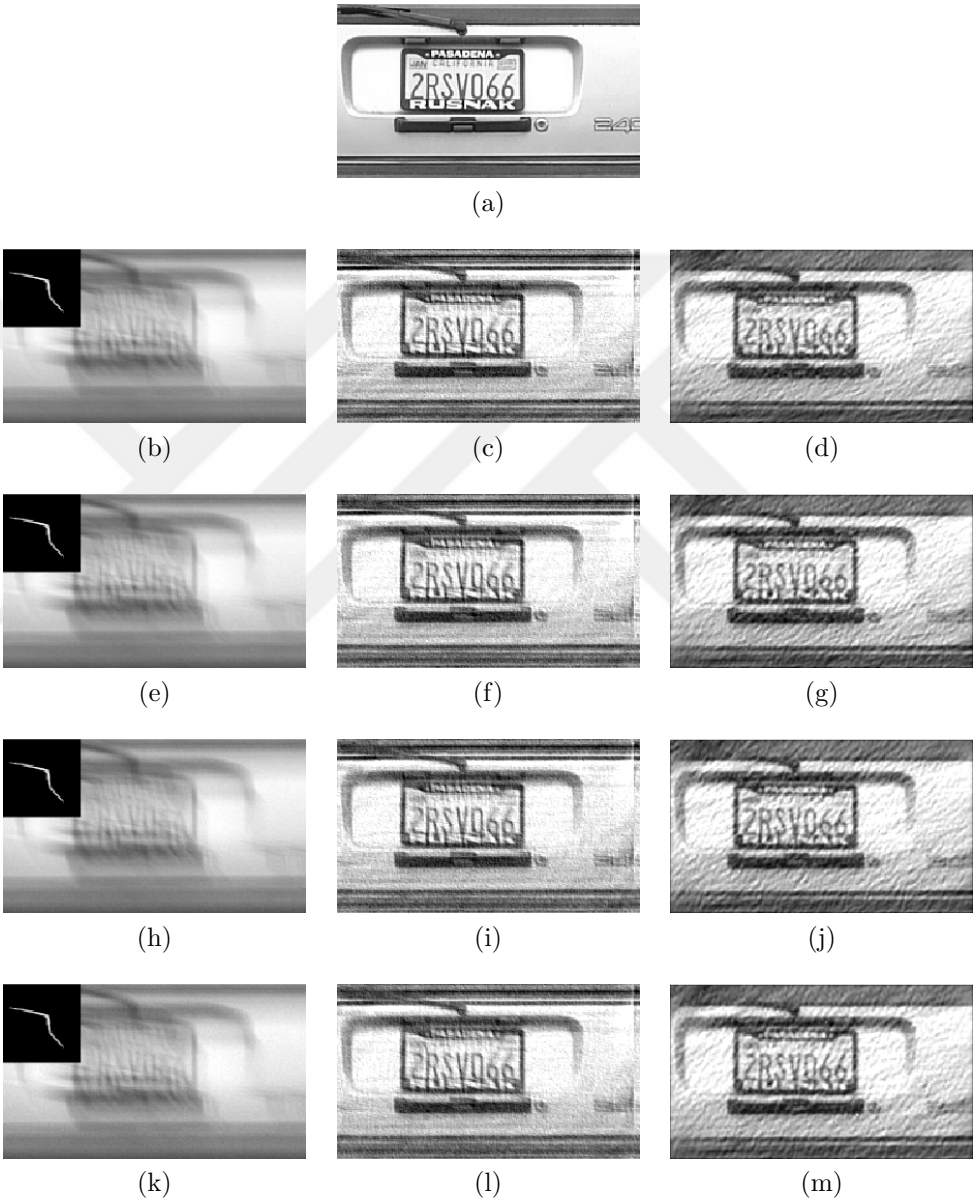
In this chapter we presented an iterative algorithm for recovering images from blurry versions that are filtered with PSFs that have complex Fourier domain coefficients. Previously described methods were designed to recover original images with symmetrical filters. With the zero phase assumption, the only requirement was the symmetry property of the filters. However, we assumed that we have a better knowledge of the filter and the proposed method is a non-blind deconvolution algorithm.

We used iterative recovery of selected Fourier domain components in order to obtain an estimate of the original image. In each iteration we successively updated phase and magnitude of of the Fourier domain image. Furthermore in spatial domain, we utilized a TV reduction algorithm in order to regularize the



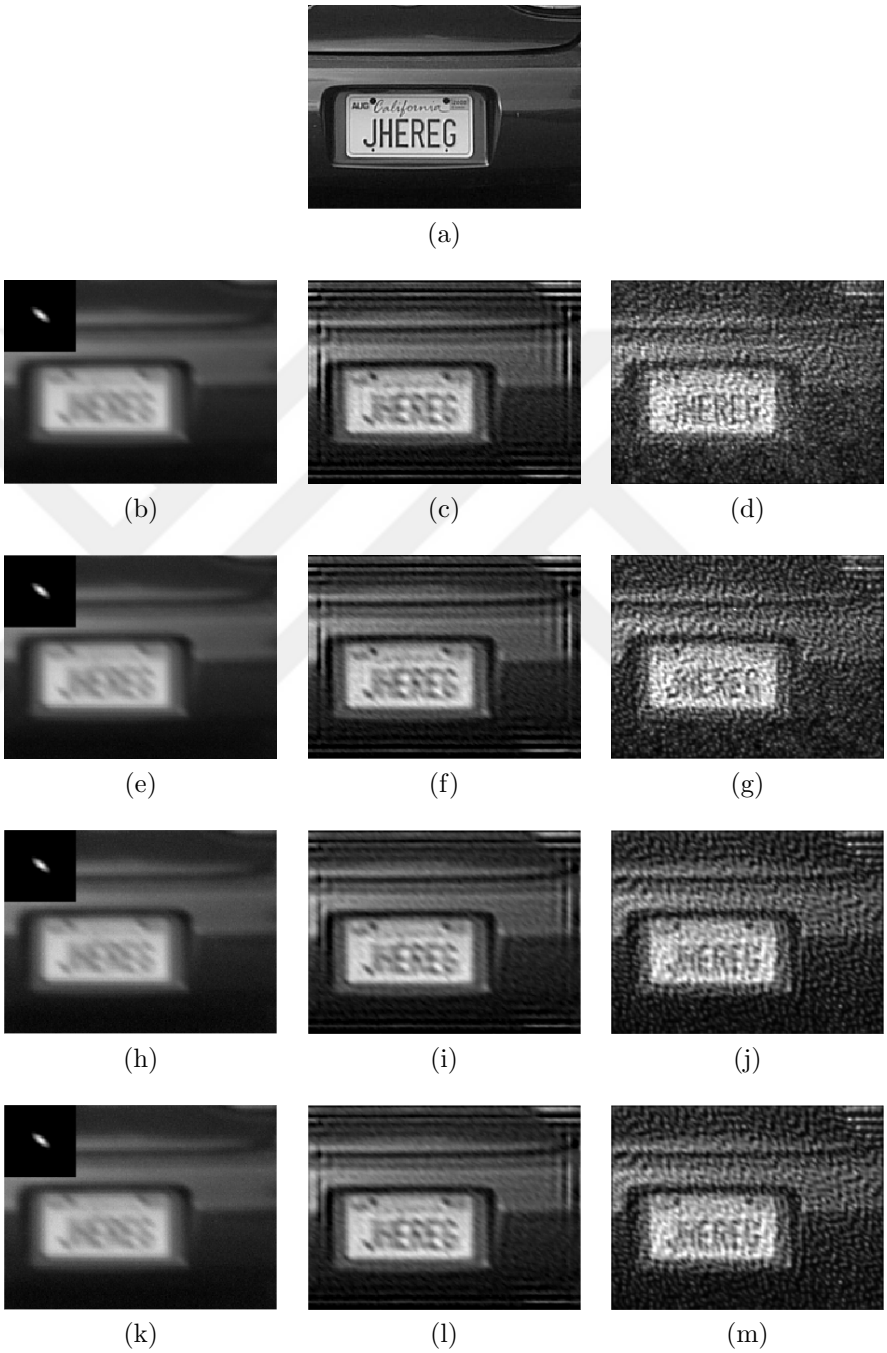
(a) (b) (c) (d) (e) (f) (g) (h) (i) (j) (k) (l) (m)

Figure 5.5: (a) A cropped portion of "image_0112.jpg". In the following four rows, images on the left are blurred versions of (a) with the PSF shown on top left corners and additive Gaussian noise with σ values: (b) 5×10^{-5}, (e) 7.5×10^{-5}, (h) 10^{-4} and (k) 1.5×10^{-4} (PSNR). The column in the middle are the results of Wiener deconvolution and the column on the right are the results of the proposed method.



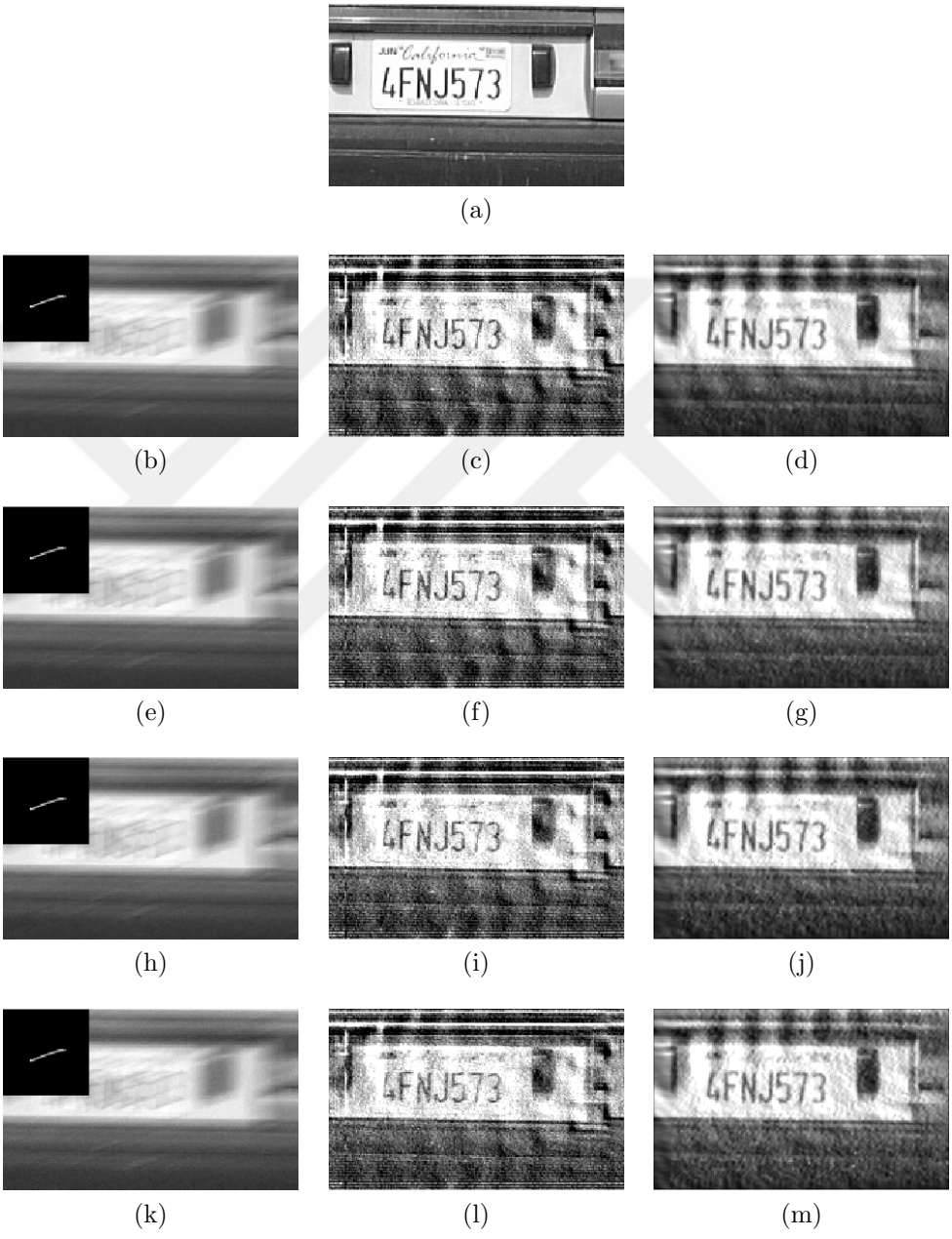
(a) (b) (c) (d) (e) (f) (g) (h) (i) (j) (k) (l) (m)

Figure 5.6: (a) A cropped portion of "image_0119.jpg". In the following four rows, images on the left are blurred versions of (a) with the PSF shown on top left corners and additive Gaussian noise with σ values: (b) 5×10^{-5}, (e) 7.5×10^{-5}, (h) 10^{-4} and (k) 1.5×10^{-4} (PSNR). The column in the middle are the results of Wiener deconvolution and the column on the right are the results of the proposed method.



(a) (b) (c) (d) (e) (f) (g) (h) (i) (j) (k) (l) (m)

Figure 5.7: (a) A cropped portion of "image_0121.jpg". In the following four rows, images on the left are blurred versions of (a) with the PSF shown on top left corners and additive Gaussian noise with σ values: (b) 5×10^{-5}, (e) 7.5×10^{-5}, (h) 10^{-4} and (k) 1.5×10^{-4} (PSNR). The column in the middle are the results of Wiener deconvolution and the column on the right are the results of the proposed method.



(a) (b) (c) (d) (e) (f) (g) (h) (i) (j) (k) (l) (m)

Figure 5.8: (a) A cropped portion of "image_0124.jpg". In the following four rows, images on the left are blurred versions of (a) with the PSF shown on top left corners and additive Gaussian noise with σ values: (b) 5×10^{-5}, (e) 7.5×10^{-5}, (h) 10^{-4} and (k) 1.5×10^{-4} (PSNR). The column in the middle are the results of Wiener deconvolution and the column on the right are the results of the proposed method.

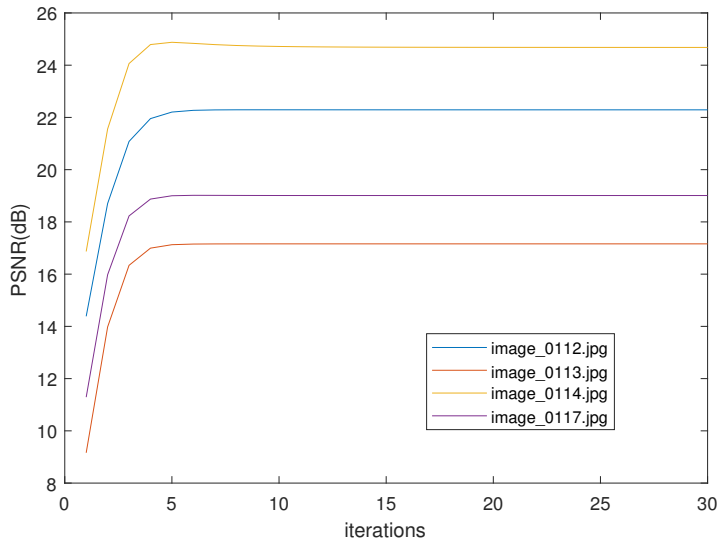


Figure 5.9: Comparison of PSNR convergence rates of four selected images versus the number of iterations.

iterate and reduce noise caused by direct replacement of Fourier phases.

The proposed method is tested against the well-known Wiener deconvolution method on a car plate image dataset. The experiments show that the proposed method outperforms the Wiener method in recovery of blurry and noisy plate images. Recent deep learning based methods are not studied in this thesis [92].

Chapter 6

Conclusions

We developed Fourier transform phase and bounded energy based blind deconvolution methods are developed. Microscopy and blurred Magnetic Particle Imaging (MPI) images are restored using the symmetry property of the point spread functions (PSF) estimated in these applications. Since the PSFs are symmetrical with respect to the origin they do not modify the Fourier phase of the original image. A computationally efficient deconvolution method is also developed for known PSF.

To the best of our knowledge, Fourier transform phase is not fully utilized in deconvolution problems. We proposed methods for extraction of Fourier transform phase of the original image from the blurry observed images. We also introduced spatial domain regularization algorithms that are used in iterative reconstruction problems. We introduced an approximate Total Variation (TV) reduction algorithm that is utilized in deconvolution iterations. We reduced the TV using a simple ℓ_1 norm projection method. TV and ℓ_1 projections regularize the inverse problem.

In both MPI and microscopy image deconvolution problems, it is assumed that the complete PSF is unknown. However the blurring process in both cases can be modelled by symmetrical filters. In microscopy images, the source of blur

is a slight shift of focus. Since the optical components are symmetrical, it is meaningful to assume the resulting blur is also symmetrical. It is assumed that the real Fourier transform coefficients created by the symmetrical property of the PSF also cause zero phase property around origin, where the great amount of information of natural images resides. Using this information for microscopic image deconvolution problem, we utilized phase constraints and integrated in the well-known iterative Ayers-Dainty blind deconvolution method as decribed in Chapter 3. Furthermore, we used a TV reduction based spatial domain constraint in order to regularize images in spatial domain. The extended blind deconvolution method is experimentally shown to outperform Ayers-Dainty algorithm.

In Chapter 4, we used a similar approach in restoration of MPI images. MPI is a new technique and it is still an active research area. Because of the physical limitations of MPI, either the resolution or the Field of View (FOV) is sacrificed in image acquisition. Large FOV is desirable, even thought such large FOV's result in highly reduced image quality. In this thesis, the symmetry property of the MPI PSF is used as a constraint in order to develop an iterative algorithm for restoration of MPI. In this case the Fourier domain phases used as Fourier constraints in iterations. We also utilized an ℓ_1 norm reduction based regularization in this algorithm. The ℓ_1 norm reduction levels the small values to zero which is desired in MPI recovery, because the contrast between the background and foreground is high. The background constitute a significant part of the image therefore TV projections are not necessary in this problem. The particles generating magnetic response is only available in the veins and images are sparse due to this reason. The simulation results of the proposed method and comparison of its MPI recovery success to the well-known Wiener and Lucy-Richardson deconvolution methods are also presented and higher quality MPI images are obtained.

In Chapter 5, we focused on a more general deconvolution case. We assumed that we were dealing with a known PSF with highly complex patterns. We do not have the zero phase property however we assume that we know the exact PSF. Therefore we use the Fourier domain magnitude and phase of the PSF in

an iterative manner to estimate and correct the Fourier coefficients of the recovered image. We again incorporate the TV reduction algorithm presented in Chapter 3 to regularize the image in spatial domain. We tested the performance of the developed algorithm using a car plate dataset. We simulated the effects of various motion-blur and camera shake PSF patterns and experimentally showed that the proposed method outperforms well-known Wiener deconvolution in recovery of such blurs with noise. The iterative phase based deconvolution method is also computationally as efficient as the Wiener deconvolution. It essentially involves an inverse DTFT computation in each iteration and our approximate TV projection requires only one division and N subtractions.

Bibliography

[1] C. Vonesch and M. Unser, "A fast multilevel algorithm for wavelet-regularized image restoration," *IEEE Transactions on Image Processing*, vol. 18, pp. 509–523, March 2009.

[2] E. Akhan, D. Tuncel, and K. C. Akcali, "Nanoparticle labeling of bone marrow-derived rat mesenchymal stem cells: their use in differentiation and tracking," *BioMed research international*, vol. 2015, 2015.

[3] D. Krishnan, T. Tay, and R. Fergus, "Blind deconvolution using a normalized sparsity measure," in *Proceedings of the IEEE Conference on Computer Vision and Pattern Recognition (CVPR)*, pp. 233–240, IEEE, 2011.

[4] M. Weber, "Cars 1999 (Rear) Dataset, Computational Vision at Caltech." `http://www.vision.caltech.edu/html-files/archive.html`. Online, Accessed: 2018-06-11.

[5] M. Sezan and H. Trussell, "Prototype image constraints for set-theoretic image restoration," *IEEE Transactions on Signal Processing*, vol. 39, pp. 2275–2285, Oct 1991.

[6] M. Sezan, "An overview of convex projections theory and its application to image recovery problems," *Ultramicroscopy*, vol. 40, no. 1, pp. 55–67, 1992.

[7] H. Trussell and M. Civanlar, "The feasible solution in signal restoration," *IEEE Transactions on Acoustics, Speech and Signal Processing*, vol. 32, pp. 201–212, Apr 1984.

[8] S. Acton, "Deconvolutional speckle reducing anisotropic diffusion," in *Proceedings of the IEEE International Conference on Image Processing (ICIP)*, vol. 1, pp. I–5–8, Sept 2005.

[9] J. Boulanger, C. Kervrann, and P. Bouthemy, "Adaptive spatio-temporal restoration for 4d fluorescence microscopic imaging," in *Medical Image Computing and Computer-Assisted Intervention – MICCAI 2005* (J. Duncan and G. Gerig, eds.), vol. 3749 of *Lecture Notes in Computer Science*, pp. 893–901, Springer Berlin Heidelberg, 2005.

[10] C. Sorzano, E. Ortiz, M. López, and J. Rodrigo, "Improved bayesian image denoising based on wavelets with applications to electron microscopy," *Pattern Recognition*, vol. 39, no. 6, pp. 1205–1213, 2006.

[11] B. Zhang, J. Zerubia, and J.-C. Olivo-Marin, "Gaussian approximations of fluorescence microscope point-spread function models," *Appl. Opt.*, vol. 46, pp. 1819–1829, Apr 2007.

[12] P. Campisi and K. Egiazarian, *Blind Image Deconvolution: Theory and Applications*. CRC press, 2007.

[13] D. Kundur and D. Hatzinakos, "Blind image deconvolution," *Signal Processing Magazine, IEEE*, vol. 13, pp. 43–64, May 1996.

[14] P. Pankajakshan, B. Zhang, L. Blanc-Féraud, Z. Kam, J.-C. Olivo-Marin, and J. Zerubia, "Blind deconvolution for thin-layered confocal imaging," *Appl. Opt.*, vol. 48, pp. 4437–4448, Aug 2009.

[15] L. Xu, S. Zheng, and J. Jia, "Unnatural l0 sparse representation for natural image deblurring," in *Proceedings of the IEEE Conference on Computer Vision and Pattern Recognition (CVPR)*, pp. 1107–1114, June 2013.

[16] P. Ye, H. Feng, Q. Li, Z. Xu, and Y. Chen, "Blind deconvolution using an improved l0 sparse representation," in *7th International Symposium on Advanced Optical Manufacturing and Testing Technologies (AOMATT 2014)*, pp. 928419–928419, International Society for Optics and Photonics, 2014.

[17] E. Bostan, U. Kamilov, M. Nilchian, and M. Unser, "Sparse stochastic processes and discretization of linear inverse problems," *IEEE Transactions on Image Processing*, vol. 22, pp. 2699–2710, July 2013.

[18] T. Chan and C.-K. Wong, "Total variation blind deconvolution," *IEEE Transactions on Image Processing*, vol. 7, pp. 370–375, Mar 1998.

[19] N. Dey, L. Blanc-Féraud, C. Zimmer, P. Roux, Z. Kam, J.-C. Olivo-Marin, and J. Zerubia, "Richardson–lucy algorithm with total variation regularization for 3d confocal microscope deconvolution," *Microscopy Research and Technique*, vol. 69, no. 4, pp. 260–266, 2006.

[20] N. Dey, L. Blanc-Féraud, Z. Christophe, R. Pascal, K. Zvi, O. J. Christophe, and Z. Josiane, "3d microscopy deconvolution using richardson-lucy algorithm with total variation regularization," *Stitud National de Recherche en Informatique et en Automatique*, vol. 7, pp. 3–43, 2004.

[21] B. Gleich and J. Weizenecker, "Tomographic imaging using the nonlinear response of magnetic particles," *Nature*, vol. 435, no. 7046, pp. 1214–1217, 2005.

[22] E. U. Saritas, P. W. Goodwill, L. R. Croft, J. J. Konkle, K. Lu, B. Zheng, and S. M. Conolly, "Magnetic particle imaging (MPI) for NMR and MRI researchers," *Journal of Magnetic Resonance*, vol. 229, pp. 116–126, 2013.

[23] P. W. Goodwill, E. U. Saritas, L. R. Croft, T. N. Kim, K. M. Krishnan, D. V. Schaffer, and S. M. Conolly, "X-space MPI: magnetic nanoparticles for safe medical imaging," *Advanced Materials*, vol. 24, no. 28, pp. 3870–3877, 2012.

[24] E. U. Saritas, P. W. Goodwill, G. Z. Zhang, and S. M. Conolly, "Magnetostimulation limits in magnetic particle imaging," *IEEE Transactions on Medical Imaging*, vol. 32, no. 9, pp. 1600–1610, 2013.

[25] E. U. Saritas, P. W. Goodwill, and S. M. Conolly, "Effects of pulse duration on magnetostimulation thresholds," *Medical Physics*, vol. 42, no. 6, pp. 3005–3012, 2015.

[26] I. Schmale, B. Gleich, J. Schmidt, J. Rahmer, C. Bontus, R. Eckart, B. David, M. Heinrich, O. Mende, O. Woywode, *et al.*, "Human pns and sar study in the frequency range from 24 to 162 khz," in *Magnetic Particle Imaging (IWMPI), 2013 International Workshop on*, pp. 1–1, IEEE, 2013.

[27] I. Schmale, B. Gleich, J. Rahmer, C. Bontus, J. Schmidt, and J. Borgert, "Mpi safety in the view of mri safety standards," *IEEE Transactions on Magnetics*, vol. 51, no. 2, pp. 1–4, 2015.

[28] O. B. Demirel and E. U. Saritas, "Effects of duty cycle on magnetostimulation thresholds in MPI," *International Journal on Magnetic Particle Imaging*, vol. 3, no. 1, p. 703010, 2017.

[29] P. W. Goodwill and S. M. Conolly, "The x-space formulation of the magnetic particle imaging process: 1-d signal, resolution, bandwidth, SNR, SAR, and magnetostimulation," *IEEE Transactions on Medical Imaging*, vol. 29, no. 11, pp. 1851–1859, 2010.

[30] P. W. Goodwill and S. M. Conolly, "Multidimensional x-space magnetic particle imaging," *IEEE Transactions on Medical Imaging*, vol. 30, no. 9, pp. 1581–1590, 2011.

[31] K. Bente, M. Weber, M. Graeser, T. F. Sattel, M. Erbe, and T. M. Buzug, "Electronic field free line rotation and relaxation deconvolution in magnetic particle imaging," *IEEE Transactions on Medical Imaging*, vol. 34, no. 2, pp. 644–651, 2015.

[32] K. Lu, P. W. Goodwill, B. Zheng, and S. M. Conolly, "Reshaping the 2d MPI PSF to be isotropic and sharp using vector acquisition and equalization," in *5th International Workshop on Magnetic Particle Imaging (IWMPI)*, IEEE, 2015.

[33] F. Lin and C. Jin, "An improved wiener deconvolution filter for high-resolution electron microscopy images," *Micron*, vol. 50, pp. 1–6, 2013.

[34] A. P. Dhawan, R. M. Rangayyan, and R. Gordon, "Image restoration by wiener deconvolution in limited-view computed tomography," *Appl. Opt.*, vol. 24, pp. 4013–4020, Dec 1985.

[35] P. Vogel, M. A. Rückert, P. Klauer, W. H. Kullmann, P. M. Jakob, and V. C. Behr, "Traveling wave magnetic particle imaging," *IEEE Transactions on Medical Imaging*, vol. 33, pp. 400–407, Feb 2014.

[36] J. B. Haldorsen, D. E. Miller, and J. J. Walsh, "Multichannel wiener deconvolution of vertical seismic profiles," *Geophysics*, vol. 59, no. 10, pp. 1500–1511, 1994.

[37] M. van der Baan, "Bandwidth enhancement: Inverse q filtering or time-varying wiener deconvolution?," *Geophysics*, vol. 77, no. 4, pp. V133–V142, 2012.

[38] M. Hayes, J. Lim, and A. V. Oppenheim, "Signal reconstruction from phase or magnitude," *IEEE Transactions on Acoustics, Speech and Signal Processing*, vol. 28, pp. 672–680, Dec 1980.

[39] A. V. Oppenheim and J. Lim, "The importance of phase in signals," *Proceedings of the IEEE*, vol. 69, pp. 529–541, May 1981.

[40] A. V. Oppenheim, M. H. Hayes, and J. S. Lim, "Iterative procedures for signal reconstruction from Fourier transform phase," *Optical Engineering*, vol. 21, no. 1, pp. 211122–211122–, 1982.

[41] S. Curtis, J. Lim, and A. V. Oppenheim, "Signal reconstruction from one bit of Fourier transform phase," in *Proceedings of the IEEE International Conference on Acoustics, Speech, and Signal Processing (ICASSP)*, vol. 9, pp. 487–490, Mar 1984.

[42] M. Tofighi, O. Yorulmaz, K. Köse, D. C. Yıldırım, R. Çetin-Atalay, and A. E. Cetin, "Phase and tv based convex sets for blind deconvolution of microscopic images," *IEEE Journal of Selected Topics in Signal Processing*, vol. 10, no. 1, pp. 81–91, 2016.

[43] O. Yorulmaz and A. E. Cetin, "Deconvolution using Fourier transform phase, ℓ_1 and ℓ_2 balls, and filtered variation," *Digital Signal Processing*, vol. 77, pp. 36–42, 2018. Digital Signal Processing and SoftwareX - Joint Special Issue on Reproducible Research in Signal Processing.

[44] N. Pustelnik, C. Chaux, and J. Pesquet, "Parallel proximal algorithm for image restoration using hybrid regularization," *IEEE Transactions on Image Processing*, vol. 20, no. 9, pp. 2450–2462, 2011.

[45] A. Chambolle, "An algorithm for total variation minimization and applications," *Journal of Mathematical Imaging and Vision*, vol. 20, pp. 89–97, Jan. 2004.

[46] M. Tofighi, K. Kose, and A. E. Cetin, "Denoising using projections onto the epigraph set of convex cost functions," in *Proceedings of the IEEE International Conference on Image Processing (ICIP)*, pp. 2709–2713, Oct 2014.

[47] Y. Censor, W. Chen, P. L. Combettes, R. Davidi, and G. Herman, "On the Effectiveness of Projection Methods for Convex Feasibility Problems with Linear Inequality Constraints," *Computational Optimization and Applications*, vol. 51, no. 3, pp. 1065–1088, 2012.

[48] P. L. Combettes and J.-C. Pesquet, "Image restoration subject to a total variation constraint," *IEEE transactions on image processing*, vol. 13, no. 9, pp. 1213–1222, 2004.

[49] P. L. Combettes and J.-C. Pesquet, "Proximal splitting methods in signal processing," in *Fixed-Point Algorithms for Inverse Problems in Science and Engineering*, Springer Optimization and Its Applications, pp. 185–212, Springer New York, 2011.

[50] A. E. Cetin, A. Bozkurt, O. Gunay, Y. H. Habiboglu, K. Kose, I. Onaran, M. Tofighi, and R. A. Sevimli, "Projections onto convex sets (POCS) based optimization by lifting," in *Proceedings of the Global Conference on Signal and Information Processing (GlobalSIP)*, pp. 623–623, IEEE, 2013.

[51] M. Tofighi, K. Kose, and A. E. Cetin, "Denoising images corrupted by impulsive noise using projections onto the epigraph set of the total variation function (PES-TV)," *Signal, Image and Video Processing*, vol. 9, no. 1, pp. 41–48, 2015.

[52] P. Brucker, "An O(n) algorithm for quadratic knapsack problems," *Operations Research Letters*, vol. 3, no. 3, pp. 163–166, 1984.

[53] J. Duchi, S. Shalev-Shwartz, Y. Singer, and T. Chandra, "Efficient projections onto the ℓ_1-ball for learning in high dimensions," in *Proceedings of the 25th International Conference on Machine Learning (ICML)*, pp. 272–279, ACM, 2008.

[54] N. Ogura and I. Yamada, "Nonstrictly convex minimization over the bounded fixed point set of a nonexpansive mapping," *Numerical Functional Analysis and Optimization*, vol. 24, no. 1-2, pp. 129–135, 2003.

[55] M. D. Altschuler, Y. Censor, G. T. Herman, A. Lent, R. M. Lewitt, S. N. Srihari, H. Tuy, and J. K. Udupa, "Mathematical aspects of image reconstruction from projections," in *Progress in pattern recognition*, pp. 323–375, Elsevier, 1982.

[56] N. E. Hurt, *Phase retrieval and zero crossings: mathematical methods in image reconstruction*, vol. 52. Springer Science & Business Media, 2001.

[57] K. Slavakis and I. Yamada, "Robust wideband beamforming by the hybrid steepest descent method," *IEEE Transactions on Signal Processing*, vol. 55, no. 9, pp. 4511–4522, 2007.

[58] K. Slavakis, S. Theodoridis, and I. Yamada, "Adaptive constrained learning in reproducing kernel hilbert spaces: the robust beamforming case," *IEEE Transactions on Signal Processing*, vol. 57, no. 12, pp. 4744–4764, 2009.

[59] S. Chouvardas, K. Slavakis, and S. Theodoridis, "Adaptive robust distributed learning in diffusion sensor networks," *IEEE Transactions on Signal Processing*, vol. 59, no. 10, pp. 4692–4707, 2011.

[60] A. Lent and H. Tuy, "An iterative method for the extrapolation of band-limited functions," *Journal of Mathematical Analysis and Applications*, vol. 83, no. 2, pp. 554–565, 1981.

[61] K. Kouris, H. Tuy, A. Lent, G. T. Herman, and R. Lewitt, "Reconstruction from sparsely sampled data by art with interpolated rays," *IEEE Transactions on Medical Imaging*, vol. 1, no. 3, pp. 161–167, 1982.

[62] A. E. Cetin, "An iterative algorithm for signal reconstruction from bispectrum," *IEEE Transactions on Signal Processing*, vol. 39, no. 12, pp. 2621–2628, 1991.

[63] A. E. Cetin, O. N. Gerek, and Y. Yardimci, "Equiripple fir filter design by the fft algorithm," *IEEE Signal Processing Magazine*, vol. 14, no. 2, pp. 60–64, 1997.

[64] A. E. Cetin and R. Ansari, "Signal recovery from wavelet transform maxima," *IEEE Transactions on Signal Processing*, vol. 42, no. 1, pp. 194–196, 1994.

[65] G. B. Unal and A. E. Çetin, "Restoration of error-diffused images using projection onto convex sets," *IEEE Transactions on Image Processing*, vol. 10, no. 12, pp. 1836–1841, 2001.

[66] A. E. Çetin and R. Ansari, "Convolution-based framework for signal recovery and applications," *JOSA A*, vol. 5, no. 8, pp. 1193–1200, 1988.

[67] The MathWorks, "Matlab image processing toolbox," Version 10.0 (R2017a). Natick, MA, USA.

[68] G. R. Ayers and J. C. Dainty, "Iterative blind deconvolution method and its applications," *Opt. Lett.*, vol. 13, pp. 547–549, Jul 1988.

[69] A. Papoulis, "A new algorithm in spectral analysis and band-limited extrapolation," *IEEE Transactions on Circuits and Systems*, vol. 22, pp. 735–742, September 1975.

[70] D. C. Youla and H. Webb, "Image restoration by the method of convex projections: Part 1 theory," *IEEE Transactions on Medical Imaging*, vol. 1, no. 2, pp. 81–94, 1982.

[71] P. Combettes, "The foundations of set theoretic estimation," *Proceedings of the IEEE*, vol. 81, pp. 182–208, Feb 1993.

[72] S. Theodoridis, K. Slavakis, and I. Yamada, "Adaptive learning in a world of projections," *Signal Processing Magazine, IEEE*, vol. 28, pp. 97–123, Jan 2011.

[73] I. Yamada, "The hybrid steepest descent method for the variational inequality problem over the intersection of fixed point sets of nonexpansive mappings," in *Inherently Parallel Algorithms in Feasibility and Optimization and their Applications* (Y. C. Dan Butnariu and S. Reich, eds.), vol. 8 of *Studies in Computational Mathematics*, pp. 473–504, Elsevier, 2001.

[74] M. Abercrombie and J. E. Heaysman, "Invasiveness of sarcoma cells," *Nature*, vol. 174, no. 4432, p. 697, 1954.

[75] J. Weizenecker, B. Gleich, J. Rahmer, H. Dahnke, and J. Borgert, "Three-dimensional real-time in vivo magnetic particle imaging," *Physics in Medicine and Biology*, vol. 54, no. 5, pp. L1–L10, 2009.

[76] K. Lu, P. W. Goodwill, E. U. Saritas, B. Zheng, and S. M. Conolly, "Linearity and shift invariance for quantitative magnetic particle imaging," *IEEE Transactions on Medical Imaging*, vol. 32, no. 9, pp. 1565–1575, 2013.

[77] P. Vogel, M. A. Rückert, P. Klauer, W. H. Kullmann, P. M. Jakob, and V. C. Behr, "First in vivo traveling wave magnetic particle imaging of a beating mouse heart," *Physics in Medicine and Biology*, vol. 61, no. 18, pp. 6620–6634, 2016.

[78] E. Y. Yu, M. Bishop, B. Zheng, R. M. Ferguson, A. P. Khandhar, S. J. Kemp, K. M. Krishnan, P. W. Goodwill, and S. M. Conolly, "Magnetic particle imaging: A novel in vivo imaging platform for cancer detection," *Nano Letters*, vol. 17, pp. 1648–1654, 2017.

[79] B. Zheng, T. Vazin, P. W. Goodwill, A. Conway, A. Verma, E. U. Saritas, D. Schaffer, and S. M. Conolly, "Magnetic particle imaging tracks the long-term fate of in vivo neural cell implants with high image contrast," *Scientific reports*, vol. 5, 2015.

[80] K. Them, J. Salamon, P. Szwargulski, S. Sequeira, M. G. Kaul, C. Lange, H. Ittrich, and T. Knopp, "Increasing the sensitivity for stem cell monitoring in system-function based magnetic particle imaging," *Physics in Medicine and Biology*, vol. 61, no. 9, pp. 3279–3290, 2016.

[81] X. Y. Zhou, K. E. Jeffris, E. Y. Yu, B. Zheng, P. W. Goodwill, P. Nahid, and S. M. Conolly, "First in vivo magnetic particle imaging of lung perfusion in rats," *Physics in Medicine and Biology*, vol. 62, no. 9, pp. 3510–3522, 2017.

[82] C. Stehning, B. Gleich, and J. Rahmer, "Simultaneous magnetic particle imaging (mpi) and temperature mapping using multi-color mpi," *International Journal on Magnetic Particle Imaging*, vol. 2, no. 2, p. 1612001, 2017.

[83] M. Utkur, Y. Muslu, and E. U. Saritas, "Relaxation-based viscosity mapping for magnetic particle imaging," *Physics in Medicine and Biology*, vol. 62, no. 9, pp. 3422–3439, 2017.

[84] L. G. C. Hamey, "A functional approach to border handling in image processing," in *Proceedings of the International Conference on Digital Image Computing: Techniques and Applications (DICTA)*, pp. 1–8, Nov 2015.

[85] M. I. Sezan and H. Stark, "Tomographic image reconstruction from incomplete view data by convex projections and direct Fourier inversion," *IEEE Transactions on Medical Imaging*, vol. 3, no. 2, pp. 91–98, 1984.

[86] H. H. Bauschke and P. L. Combettes, *Convex Analysis and Monotone Operator Theory in Hilbert Spaces*. Springer, 2011.

[87] M. R. Civanlar and H. J. Trussell, "Constructing membership functions using statistical data," *Fuzzy Sets and Systems*, vol. 18, pp. 1–13, Jan 1986.

[88] H. Trussell and M. Civanlar, "The landweber iteration and projection onto convex sets," *IEEE Transactions on Acoustics, Speech, and Signal Processing*, vol. 33, pp. 1632–1634, Dec 1985.

[89] R. M. Ferguson, A. P. Khandhar, S. J. Kemp, H. Arami, E. U. Saritas, L. R. Croft, J. Konkle, P. W. Goodwill, A. Halkola, J. Rahmer, *et al.*, "Magnetic particle imaging with tailored iron oxide nanoparticle tracers," *IEEE Transactions on Medical Imaging*, vol. 34, no. 5, pp. 1077–1084, 2015.

[90] L. R. Croft, P. W. Goodwill, J. J. Konkle, H. Arami, D. A. Price, A. X. Li, E. U. Saritas, and S. M. Conolly, "Low drive field amplitude for improved

image resolution in magnetic particle imaging," *Medical Physics*, vol. 43, no. 1, pp. 424–435, 2016.

[91] L. R. Croft, P. W. Goodwill, and S. M. Conolly, "Relaxation in x-space magnetic particle imaging," *IEEE Transactions on Medical Imaging*, vol. 31, no. 12, pp. 2335–2342, 2012.

[92] G. Litjens, T. Kooi, B. E. Bejnordi, A. A. A. Setio, F. Ciompi, M. Ghafoorian, J. A. van der Laak, B. Van Ginneken, and C. I. Sánchez, "A survey on deep learning in medical image analysis," *Medical image analysis*, vol. 42, pp. 60–88, 2017.